DPST-78-128-5/6

SAVANNAH RIVER LABORATORY MONTHLY REPORT

^{238}Pu FUEL FORM PROCESSES MAY/JUNE 1978

SAVANNAH RIVER LABORATORY
AIKEN, SOUTH CAROLINA 29801

PREPARED FOR THE U.S. DEPARTMENT OF ENERGY UNDER CONTRACT AT(07-2)-1

DISCLAIMER

DPST-78-128-5/6

SAVANNAH RIVER LABORATORY MONTHLY REPORT

^{238}Pu FUEL FORM PROCESSES MAY/JUNE 1978

Approved by:

R. T. Huntoon, Research Manager
Nuclear Materials Division

E. I. DU PONT DE NEMOURS AND COMPANY
SAVANNAH RIVER LABORATORY
AIKEN, SOUTH CAROLINA 29801

PREPARED FOR THE U. S. DEPARTMENT OF ENERGY UNDER CONTRACT AT(07-2)-1

CONTENTS

FOREWORD

This report is one of a series to summarize progress in the Savannah River ^{238}Pu Fuel Form Program. This program is supported primarily by the DOE Division of Advanced Systems and Materials Production (DASMP), and also by the Division of Military Applications (DMA).

Goals of the Savannah River Laboratory (SRL) program are: to provide technical support for the transfer of DASMP and DMA ^{238}Pu fuel form fabrication operations from Mound Laboratory to new facilities at the Savannah River Plant (SRP), to provide the technical basis for ^{238}Pu scrap recovery at SRP, and to assist in sustaining plant operations. This part of the program includes:

Demonstration of processes and techniques, developed by the Los Alamos Scientific Laboratory (LASL) and Monsanto Research Corporation (MRC), for production at SRP. Information from the demonstration will provide the technical data for technical standards and operating procedures.

Technical Support to assist plant startup and to ensure continuation of safe and efficient production of high-quality heat-source fuel.

Technical Assistance after startup to accommodate changes in product and product specifications, to assist user agencies in improving product performance, to assist SRP in making process improvements that increase efficiency and product reliability, and to adapt plant facilities for new products.

MULTI-HUNDRED WATT PROCESS DEMONSTRATION

MICROSTRUCTURAL ANALYSIS OF SPHERES 3 AND 13

Microstructural studies of the unfractured and dimensionally stable Spheres 3 and 13 confirmed that the two methods previously suggested[1] to alter the LASL process for PuFF application are successful in retaining shard integrity and intershard porosity in MHW spheres. Either the load during hot pressing may be reduced[2] or the shard sintering temperature may be increased to accommodate the higher effective pressure of the double-action (PuFF) versus single-action (LASL) press. Large variations in density (≥12% TD) were observed within these spheres with the highest densities in the equatorial region. Cracks were observed in the high-density areas (>87% TD) in which the shards had been crushed. Density gradients must therefore be reduced significantly to produce a sphere of 82.5% bulk density without regions exceeding 85-87% TD, the previously observed threshold density for cracking.[1,2,3]

This microstructural study is part of a continuing examination by SRL of preproduction spheres being fabricated in the PuFF Facility to assess the causes of excessive fracture and shrinkage in the earlier PuFF spheres. Spheres 3 and 13 were selected for microstructural analysis and comparison because these spheres were representative of those significant variations in critical production parameters that were beneficial in obtaining more stable spheres.[1,2,4] The microstructures of Spheres 3 and 13 were compared with the microstructure of Sphere 4, which was typical of the generally dense and fractured Spheres 1-10 produced at SRP according to the LASL flowsheet. The microstructure of Sphere 4, however, was not characteristic of the typical LASL microstructure. The double-action press at SRP apparently produces a higher effective pressure than does the single-action press used by LASL to develop the MHW process. The high effective pressure crushed the shards and eliminated coarse intershard porosity. These conditions caused excessive shrinkage, regions of high density, and hence fracture in Spheres 1-10.

The process variables compared in this analysis were hot-press pressure (Sphere 13) and extent of shard sintering (Sphere 3). Sphere 13 was hot pressed with a lower pressure (1500 vs. 3000 psi) and a lower load application rate than used in the LASL process.[1,2] The hot pressing conditions used for subsequent sphere production in PuFF have been based on the successful results

of Sphere 13. Sphere 4 was fabricated according to the standard LASL-MHW flowsheet (shards sintered 5 hr at 1175°C and then hot pressed at 3000 psi). Shards for Sphere 3 were sintered at higher temperatures (>1200°C) and for longer times (<12 hr vs. 5 hr) than required by the LASL process. Small differences in other processing steps were not considered to have a significant effect on the micro-structure of these spheres.

Sphere 13

A microstructural analysis of Sphere 13 was made to evaluate the following characteristics: shard integrity, pore size and spatial distribution, shard density, density gradients, cracking, impurities, and grain size. Sphere 13 was hot pressed with a reduced load.[2] In contrast to earlier PuFF spheres, only one surface crack appeared during reoxidation, the integrity of the sphere was maintained, and shrinkage was not excessive.

Shard Structure

Microstructural analysis of the cross section of Sphere 13 from the top pole to the center showed that the shard identity was maintained along this radius (Figure 1). A section of Sphere 13, believed to be from the equatorial region, showed a significantly different microstructure from that of the polar radius. The effective pressure in the equatorial region was sufficient to crush the shards and destroy the shard structure (Figure 2). However, the relative volume of crushed shards in Sphere 13 was much less than in earlier spheres pressed at higher pressures and loading rates.

Porosity

The characteristics of pores (size, shape, concentration, and spatial distribution) strongly influence the properties of MHW spheres. The pore structure controls shrinkage, provides channels for internal gas release (He, CO, CO_2), may relieve strain energy from internal stresses, and may also blunt microcracks. The characteristics of the shards in the sintered microstructure strongly influenced the pore size. When the shard integrity was maintained, as it was along the polar radius, three types of porosities were observed (Figure 3). Although pore size distributions were not measured quantitatively, size ranges could be determined from micrographs. One type of porosity was in the form of large, stabilizing, triple-point pores at the intersection of three or more shard boundaries and was 10 to 50 μm in diameter. Another of the observed porosity types was in the form of intershard pores along shard boundaries with a size range of 2 to 10 μm. As the effective pressure increased (higher-density areas), the size of intershard pores decreased, and many of these pores were eliminated. At even

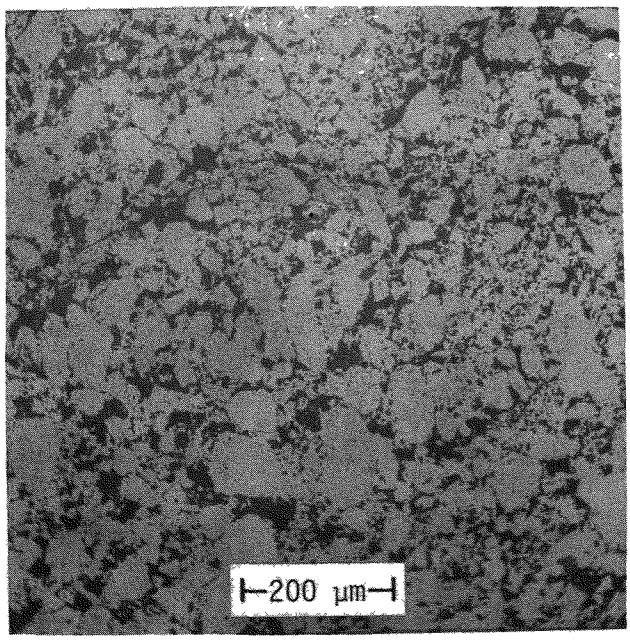

a. 0.08 in. from Top Surface

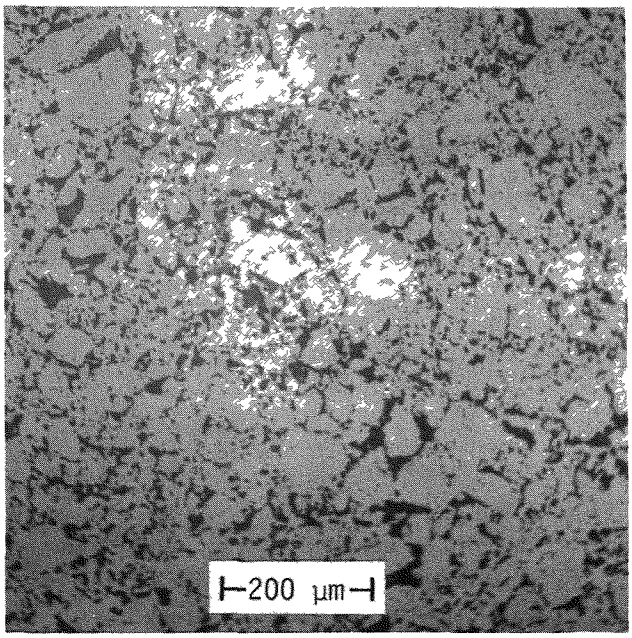

b. 0.31 in. from Top Surface

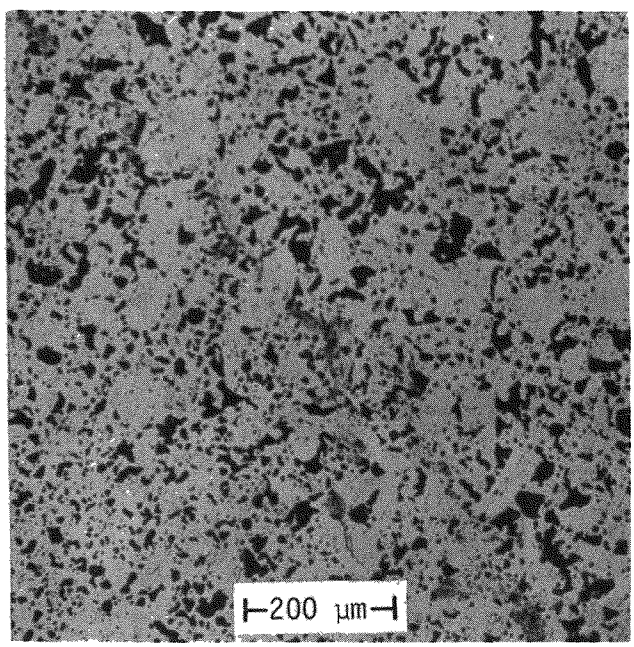

c. 0.67 in. from Top Surface

FIGURE 1. Microstructure of Cross Section of Sphere 13 from Top Pole to Center Along Polar Radius (As Polished)

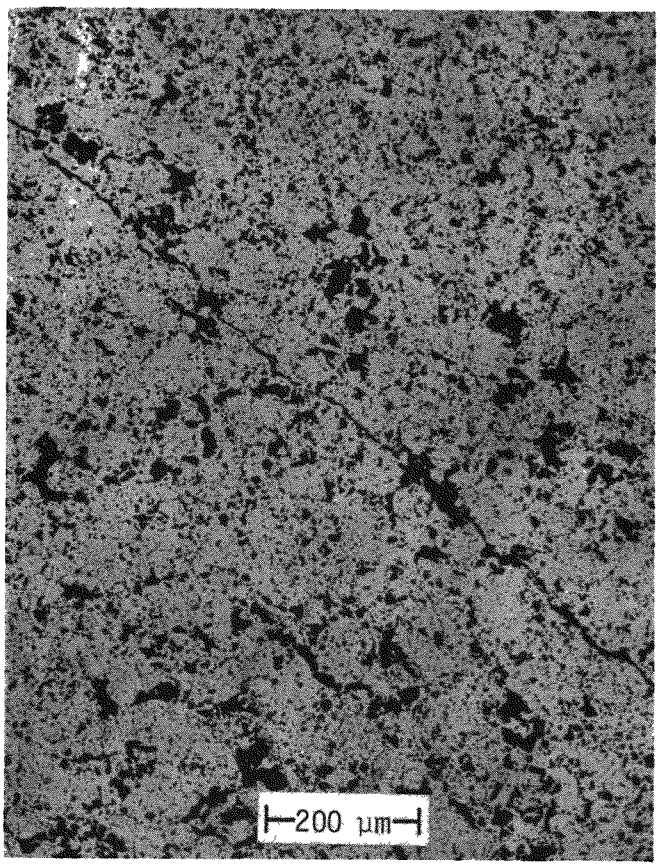

FIGURE 2. Microstructure of Sphere 13 in Equatorial Region (As Polished)

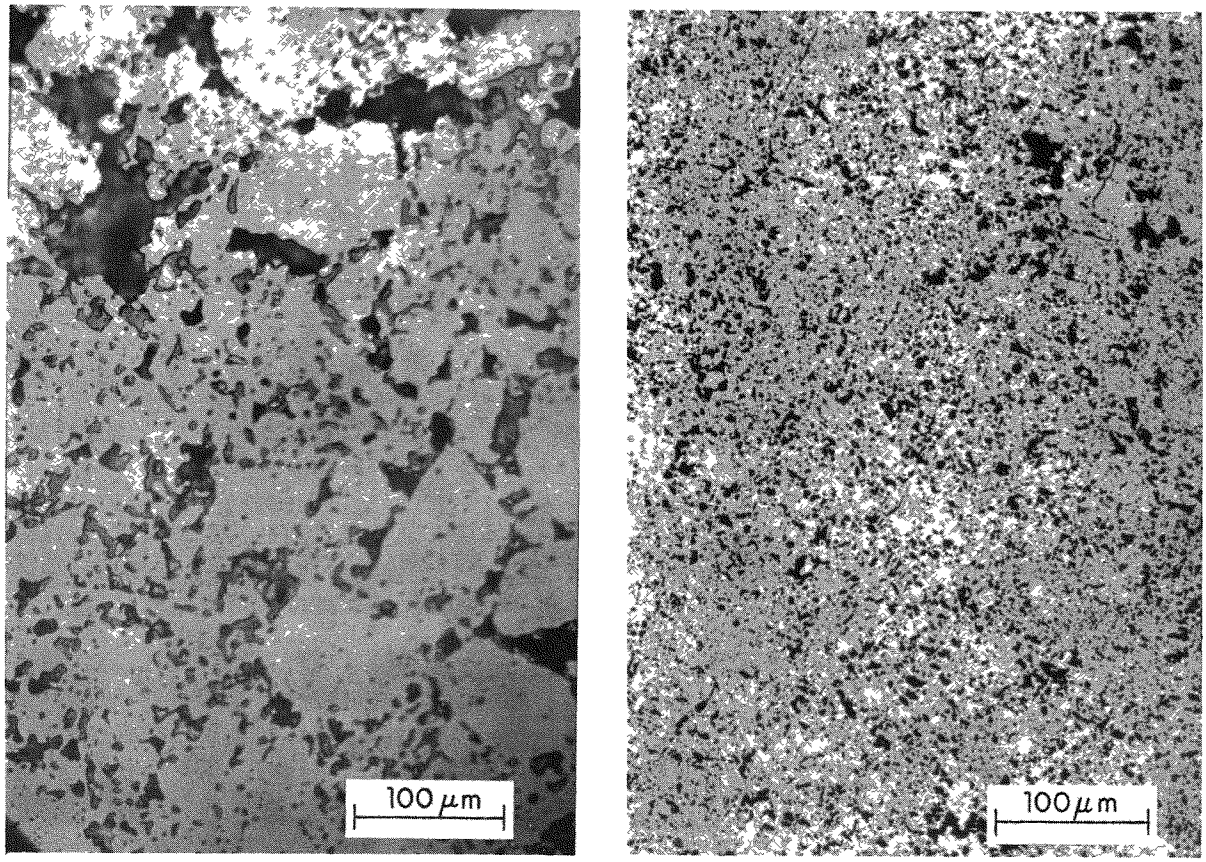

Polar Region

Equatorial Region

FIGURE 3. Sphere 13 Pore Size Distribution (As Polished)

higher effective pressures, as encountered in the equatorial region, shards were crushed, and the pore size distribution was drastically altered. The pore size distribution was more continuous, rather than tri-modal, and most of the pores were less than 15 μm (Figure 3).

A third type of porosity is intrashard porosity. Pores observed within shards, usually at grain boundaries, were less than 2 μm in diameter. The concentration of intrashard pores was higher near the top polar surface than within the interior of Sphere 13 as shown in Figure 4. This change in the concentration of intrashard pores caused a shard-density gradient along the polar axis. Shards near the top polar surface of Sphere 13 had an internal density of 89-91% TD. Shard densities at the interior of the spheres were 94-97% TD.

Density Variation

A substantial variation in density existed within Sphere 13. The density gradient, measured along the polar radius from photomicrographs was 87-76% TD, as shown in Figure 5. The density distribution shown in Figure 5 is similar to but not as steep as that observed for Sphere 4 (Figure 19 of the January-February 1978 report[1]). Also, peak and average densities for Sphere 13 were less than for Sphere 4. The average density of Sphere 13 was 84.2% TD[2] as determined from weight and size measurements. The average metallographic density along the polar radius was only 82.4% TD. The average metallographic density in the equatorial region was 87.9% TD. These density gradients result from differences in effective pressure created by the unequal distribution of force in spherical compaction and by frictional forces between shards which inhibit the flow and rearrangement of the shards. Density variations tend to increase internal stresses from thermal gradients, reoxidation effects, and differential sintering, all of which can play a role in causing fracture in spheres.

Previous work has indicated that cracking in MHW spheres appears to occur above a threshold density of about 85-87% TD.[1,2,3] The location, incidence, and characteristics of cracks observed in Sphere 13 are essentially consistent with these earlier observations. Cracks were observed in the equatorial region of Sphere 13, which had an average metallographic density of 87.9% TD and contained crushed, closely compacted shards (Figure 6). Although densities approaching 87% TD were measured along the polar radius, few cracks were observed. Grain-boundary separations and microcracks within shards were observed, but most of these microcracks did not propagate across shard boundaries. Relatively large pores at shard boundaries can act to blunt microcracks and may have inhibited the propagation of these cracks across shard boundaries.

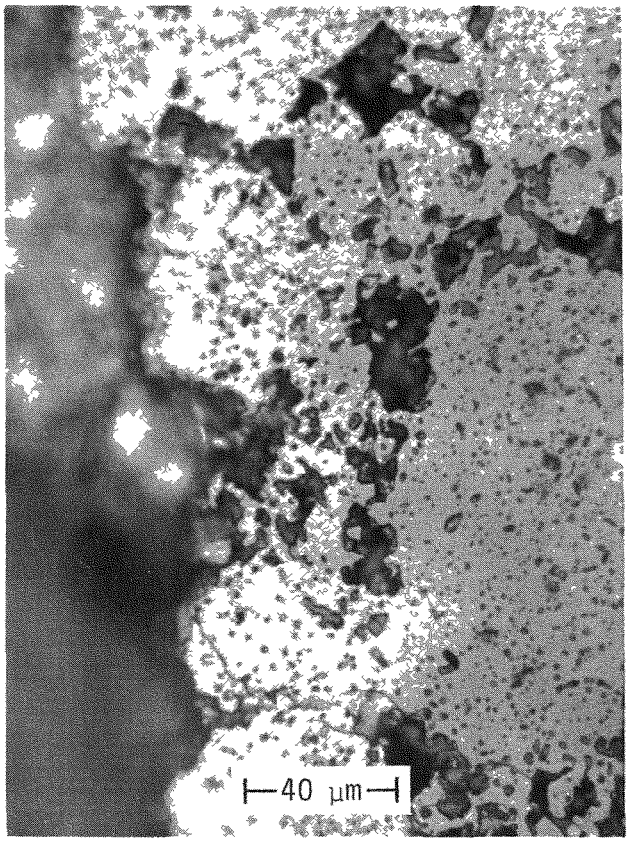

a. Top Polar Surface, 90%-TD Shards

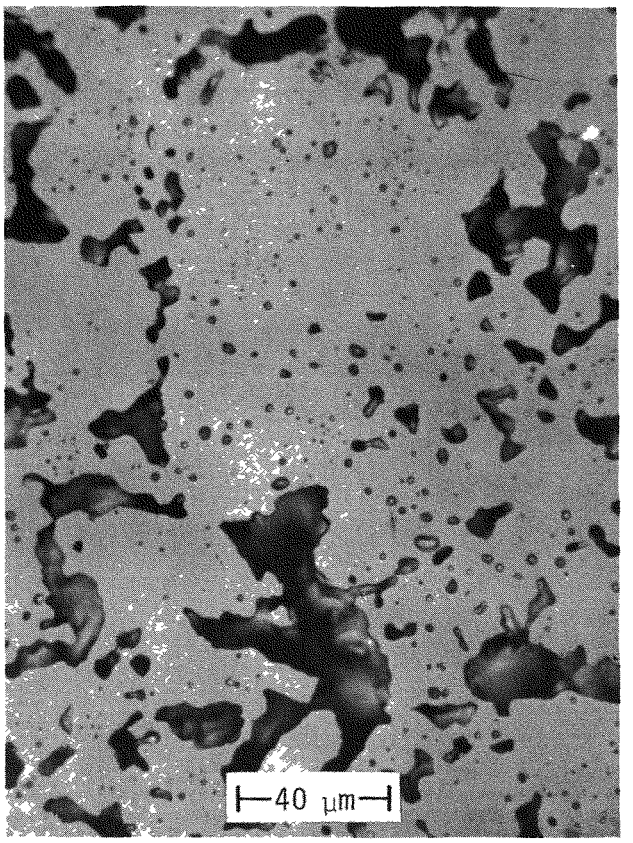

b. 0.31 in. from Top Pole Along Polar Radius, 95%-TD Shards

FIGURE 4. Intrashard Porosity of Sphere 13 (As Polished)

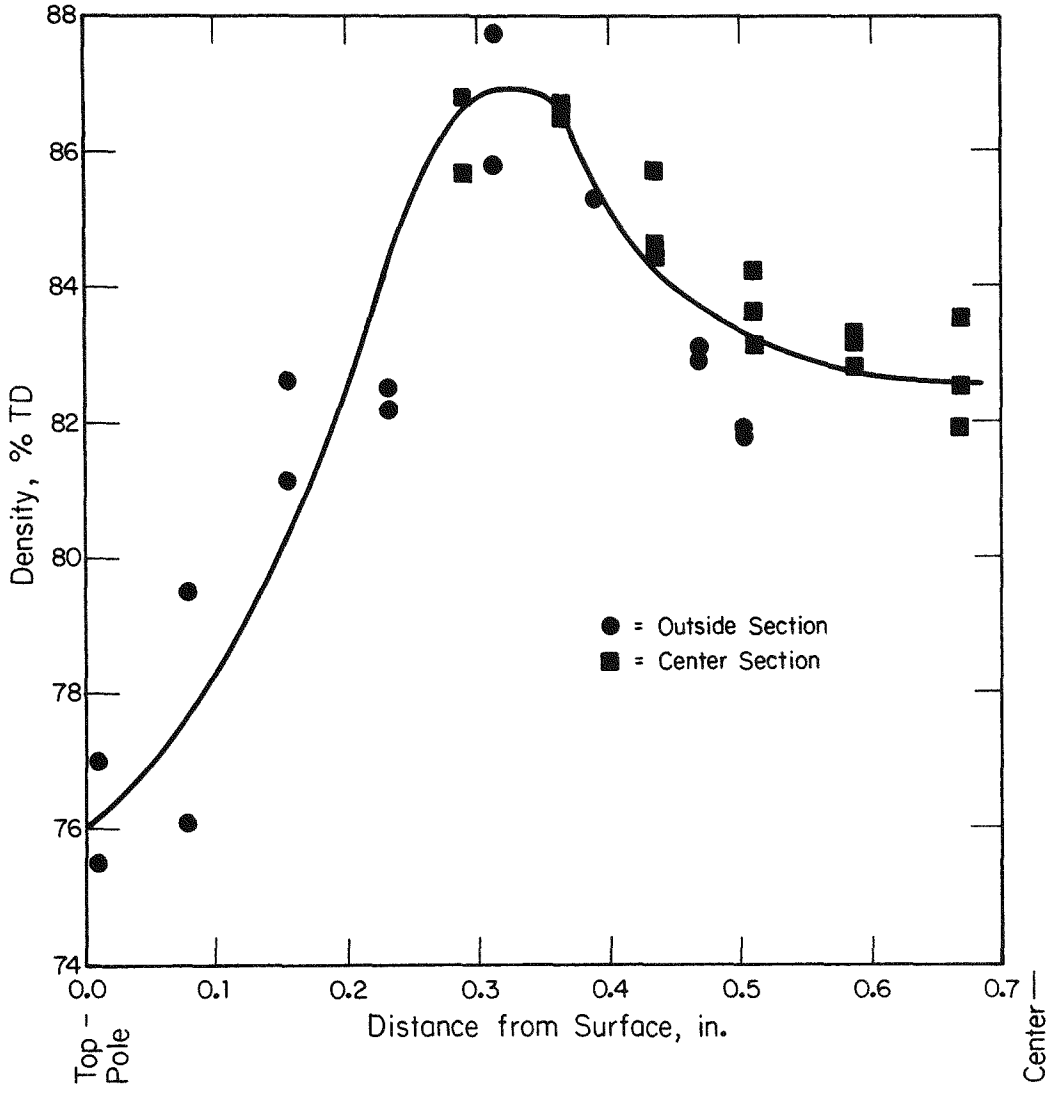

FIGURE 5. Density Gradient in Sphere 13, Top Pole to Center

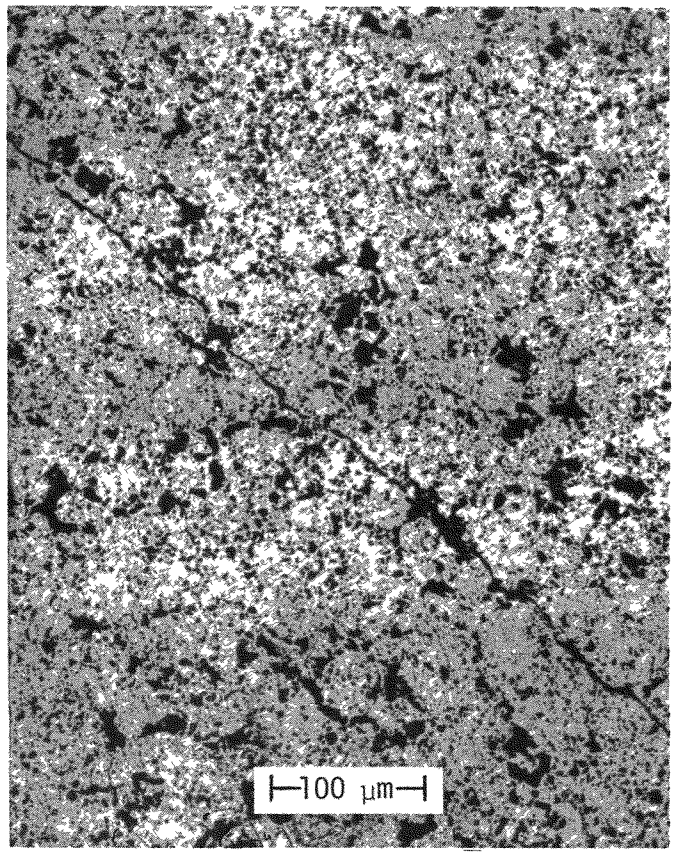

FIGURE 6. Crack in Equatorial Region of Sphere 13 (As Polished)

Pores may also act to relieve strain energy from internal stresses. Both of these factors probably help prevent degradation of the sphere. Cracking in Sphere 13 correlates directly with the elimination of the shard structure and intershard porosity at densities greater than 87% TD.

Grain Size

A grain-size gradient along the polar axis was apparent when as-polished sections were acid etched to reveal the grain boundaries. The grain structures of different regions of Sphere 13 are shown in Figure 7. The grain size at the top pole was 10 to 15 μm. The grain size in the interior of the radial segment was about 25 to 50 μm. In the section observed from near the equator, the grain size was 15 to 25 μm. The variables affecting rate of grain growth in the sphere are pore size and concentration (primarily intrashard pores) and temperature. The cause of grain-size variations in Sphere 13 may be attributed to variations in pore size and concentration and to thermal gradients from self-heating.

Impurities

A small concentration of heterogeneously distributed impurities, probable Fe, were observed in many of the micrographs of Sphere 13. These impurities appeared to be similar to those observed in other spheres, as described previously[1] and elsewhere in this report. Most impurities were in the 2- to 5-μm size range. The impurities had little effect on the microstructure and did not appear to be a source of microcracks.

Sphere 3

A metallographic study of sections of Sphere 3 (November/December 1977 report[4]) was also made. The sintering temperature of the shards used to fabricate this sphere was at least 1240°C and probably much higher as evidenced by the higher density of the shards. The higher-density shards would have a higher compressive strength which would account for the improved microstructure as shown in Figure 8. The identities of many of the shards were retained. Other shards apparently were still crushed by the relatively high compressive force used to press Sphere 3. The resulting microstructural features, including shard identity, pore size, and metallographic density, were generally intermediate between those of Spheres 4 and 13. In some regions the trimodal pore size distribution was preserved. However, pores of intermediate size were produced in regions where shards were crushed. Metallographic densities ranged from 76 to over 97% TD in the sections observed. The incidence of cracking in Sphere 3 was also intermediate between that of Spheres 13 and 4, although cracking was much more prevalent than for Sphere

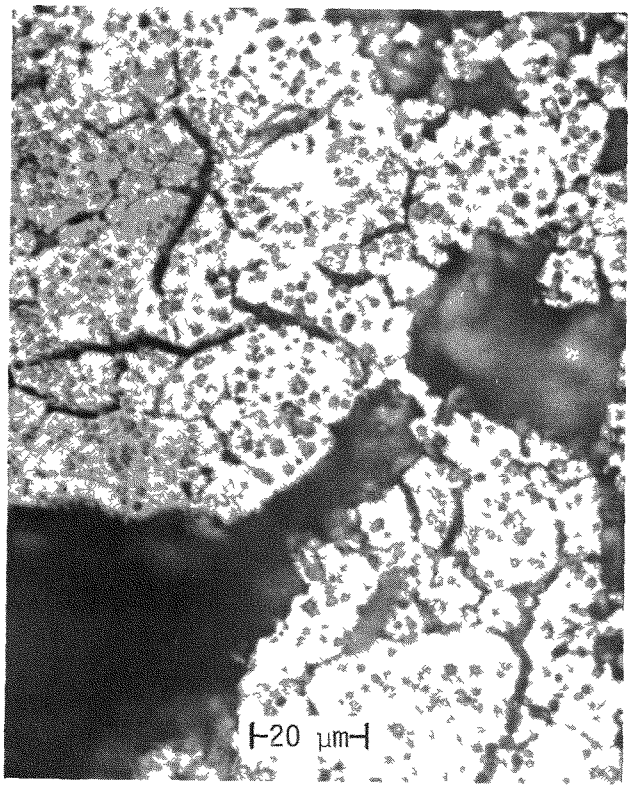

Top Polar Surface

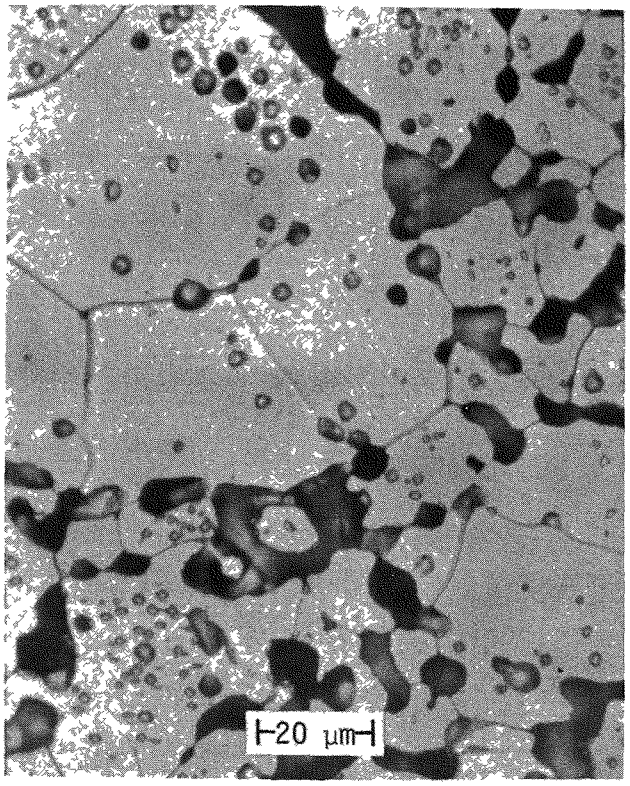

0.4 in. from Top Pole
Along Polar Radius

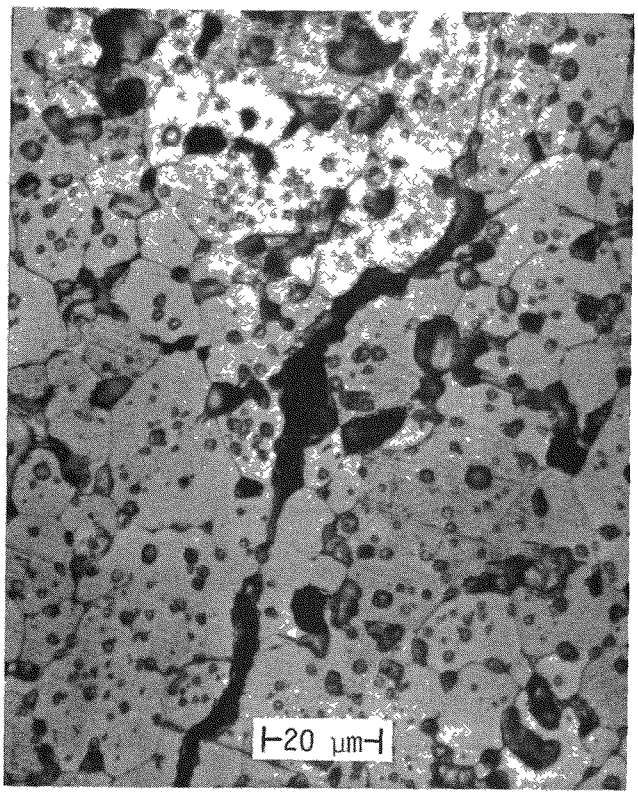

Equatorial Region

FIGURE 7. Grain-Size Variations in Sphere 13 (Acid Etched)

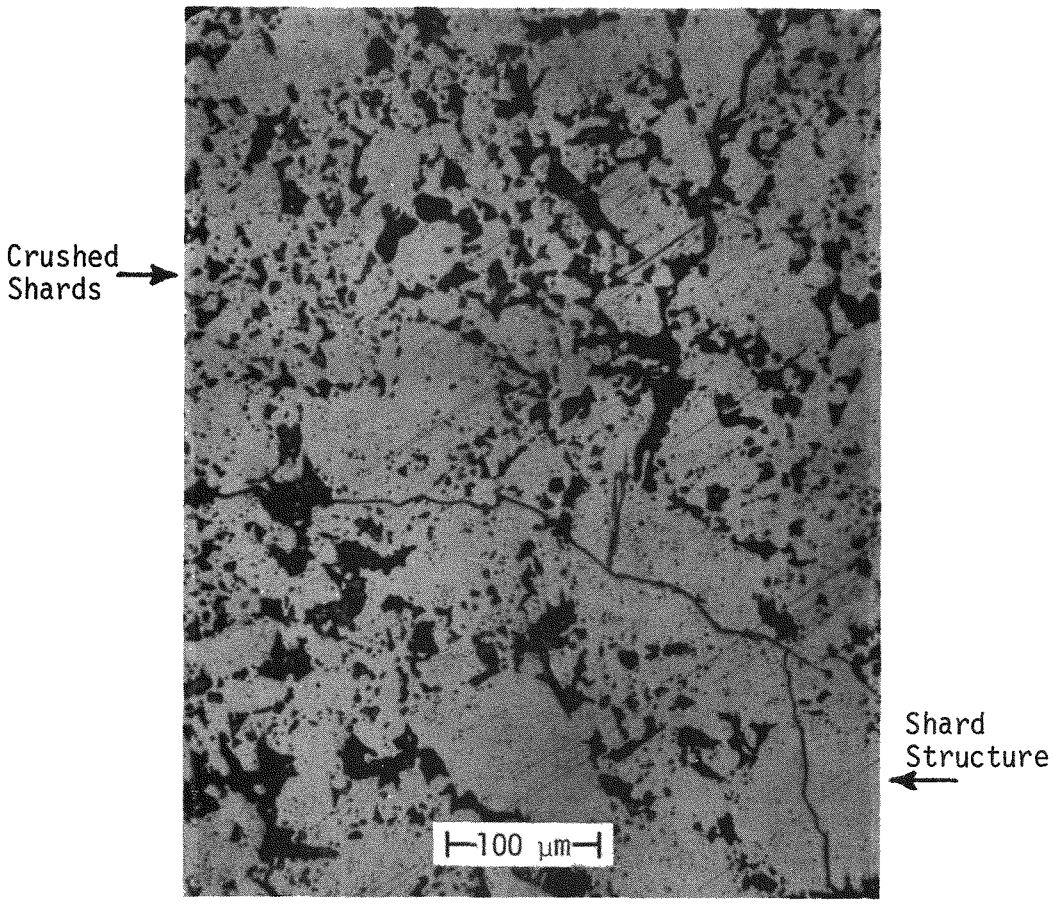

FIGURE 8. Typical Improved Microstructure
(Sphere 3, As Polished)

13. Because Sphere 3 was thermally cycled numerous times after fabrication, many of the cracks observed may have been caused by thermal shock.

A relatively large concentration of impurities, probably Fe, was detected in Sphere 3 (Figure 9). These impurities appear to be at shard boundaries. Strings of these impurities may have been the source of some of the cracks observed in Sphere 3.

A range of grain sizes of 5 to 25 μm was measured in the section of Sphere 3 that was examined.

Comparison of Microstructures of Spheres 3 and 13 with Sphere 4

Sphere 4, which was representative of Spheres 1-10, was fractured and too dense. A brief summary of the microstructure is presented here for comparison with Spheres 3 and 13. Examination along the polar radius of Sphere 4 revealed that the shard structure was retained at the top polar surface (Figure 19 of the January/February 1978 report[1]) as it was in Spheres 3 and 13. However, the increase in density towards the center of Sphere 4 was much more rapid than in Sphere 13. Excessive densities and cracking were observed in the equatorial regions of Spheres 4 and 13, but the density was higher and the cracks were more severe in Sphere 4. Radial tensile cracks were also observed at the top polar surface extending into the high-density interior of Sphere 4. Tensile stresses in the surface of spheres result from volume changes during reoxidation and from thermal gradients and/or differential sintering along density gradients. The primary cause of cracking in high-density areas is believed to be internal stresses created by volume changes and gas pressure during reoxidation.[1,3]

The concentration and size of impurities were greater in both Spheres 3 and 4 than in Sphere 13.

IRON IMPURITIES IN PuFF SPHERES

Heterogeneously distributed impurities were observed in all fragments of the spheres examined by metallographic analyses (Spheres 1, 4, and 5 described previously[1] and Spheres 3 and 13 described elsewhere in this report). These impurities have been identified as being metallic and principally iron by scanning electron microscopy and associated x-ray energy spectroscopy. On the basis of composition, size, shape, abundance, and intershard distribution of the impurities, they are believed to be

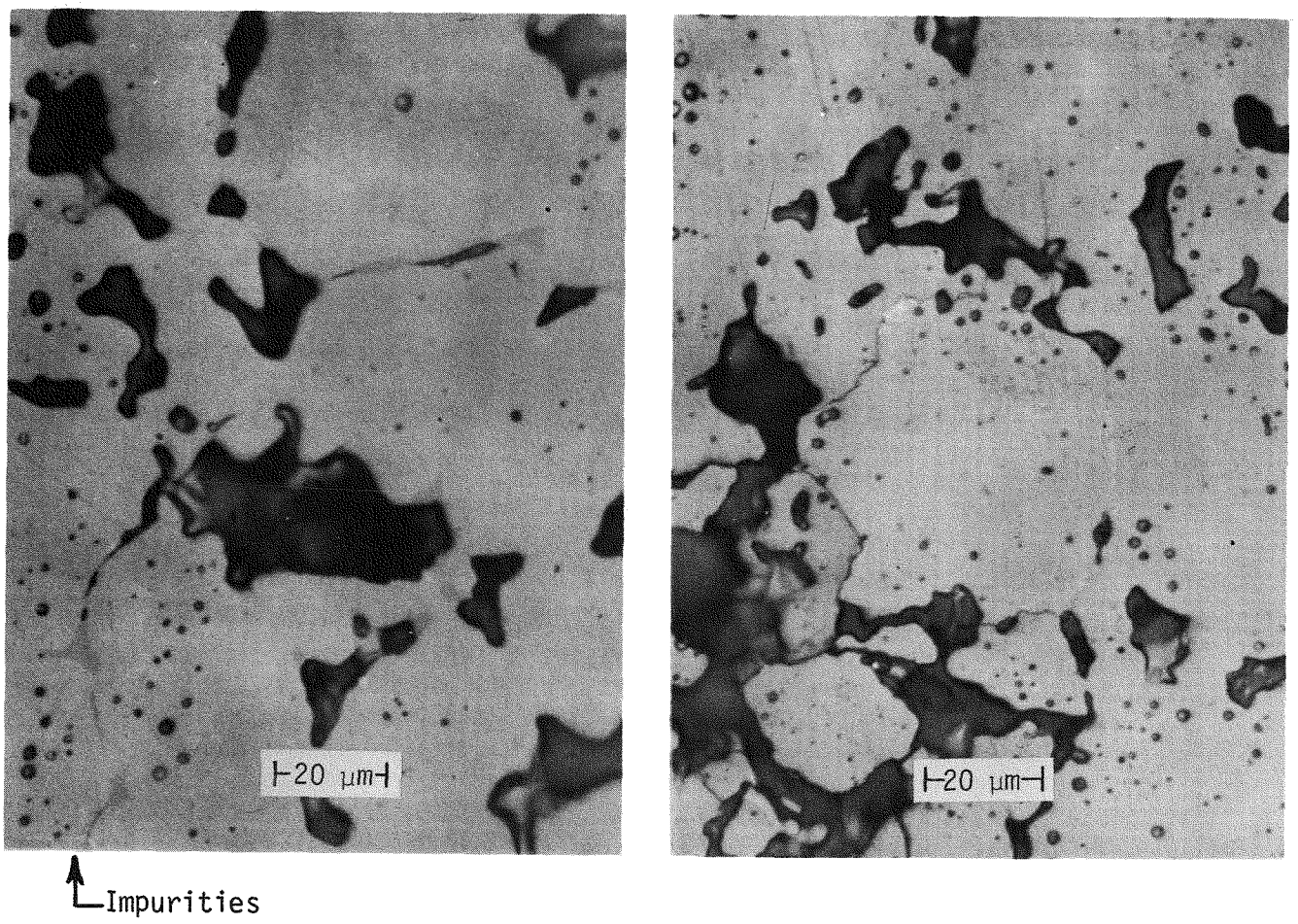

FIGURE 9. Impurities in Sphere 3 (As Polished)

bristle fragments from the steel brushes used to comminute compacts into shards by crushing through a screen. The impurity concentration in Sphere 13, although not quantitatively measured, was much lower than in previous spheres.

Typical impurities are shown in Figures 21 and 22 of the January/February 1978 report[1] and in Figure 9 of this report. A representative example of the impurities is shown in Figure 10. This sample, taken from Sphere 4, was analyzed as-polished for impurities as shown in Figures 11 and 12. Region 1 in Figures 10 and 11 consists of an area of metallic impurity (appears white in Figure 10) surrounded by a shoulder of gray. The white area was determined to be predominately iron (Figure 11). There was no evidence of iron in the surrounding matrix (Figure 11). The large white impurity of Region 2 (Figure 10) was also analyzed and found to be predominantly iron (Figure 12). Other potential impurities such as Cr, Ni, Ca, Si, Al, or Mg were not detected.

The gray shoulder surrounding the metallic areas contained no evidence of iron or other impurities and appears to be a recessed empty cavity (Figure 11). One possible explanation for the gray shoulder is that the iron impurity melted during hot pressing and then, during cooldown, solidified and shrunk away from the PuO_2 matrix creating a void. As was suggested previously,[1] these gray areas possibly represented nonmetallic impurities such as furnace refractories. On the basis of this analysis, however, the gray areas appear to be voids created by the solidification and shrinkage of molten iron during cooldown after hot pressing or, perhaps, removal on grinding or polishing the surface. Consequently, only iron impurities produce the two textures of impurities observed by SEM.

The iron impurities are postulated to be introduced during shard preparation, probably from broken bristles from the steel brush used to force cold-pressed compacts through a steel screen. The impurities occur heterogeneously and are located primarily on shard boundaries, indicating their addition occurs during the sharding process rather than in the B-Line feed or in milling. The large, elongated piece of iron in Figure 10, Region 2, has a width of 50 μm (∿0.002 in.) which is reasonable for a bristle diameter cut on a chord. The distribution of the impurity indicates preferential location at shard boundaries (Figure 9

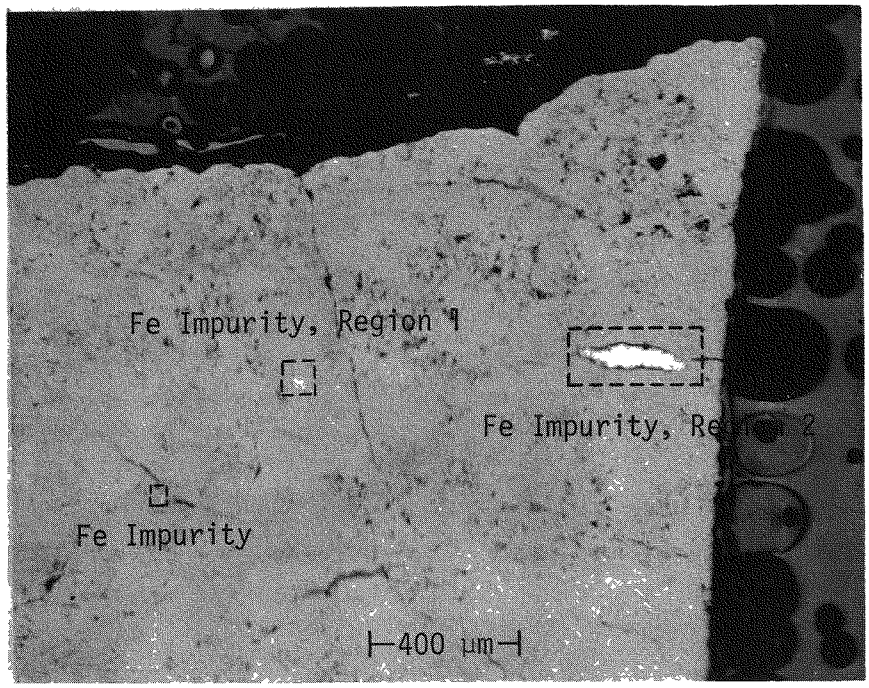

FIGURE 10. Iron Impurities in Plutonia Matrix of Sphere 4

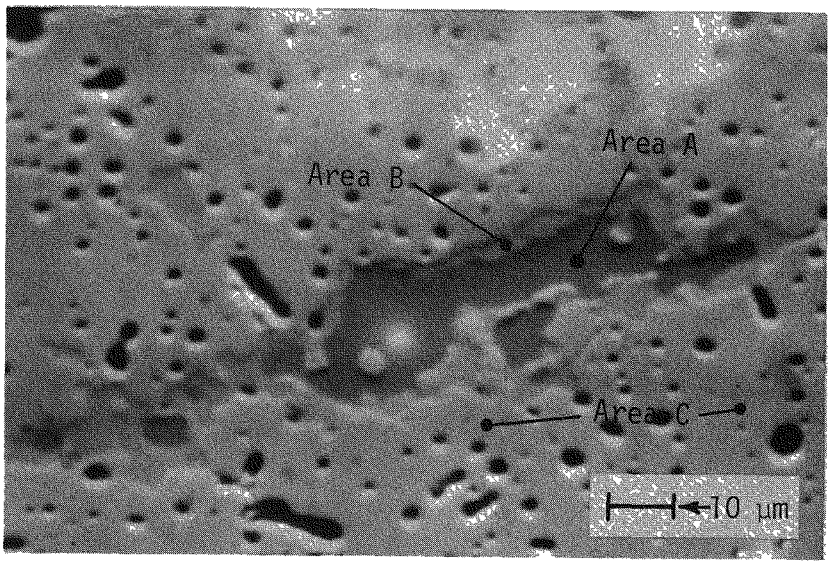

Region 1

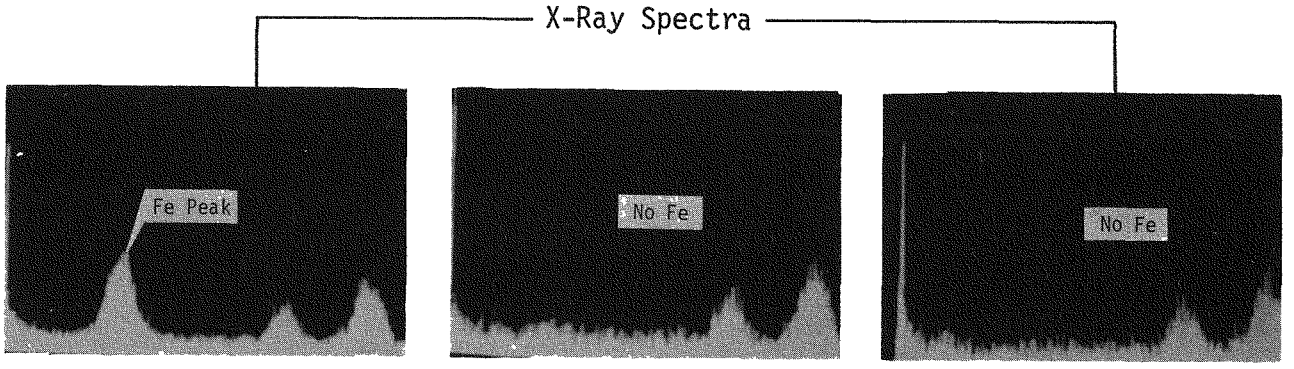

a. Area A (White Impurity)

b. Area B (Shoulder)

c. Area C (Matrix)

FIGURE 11. Fe Impurity in Sphere 4 Surrounded by Plutonia Matrix

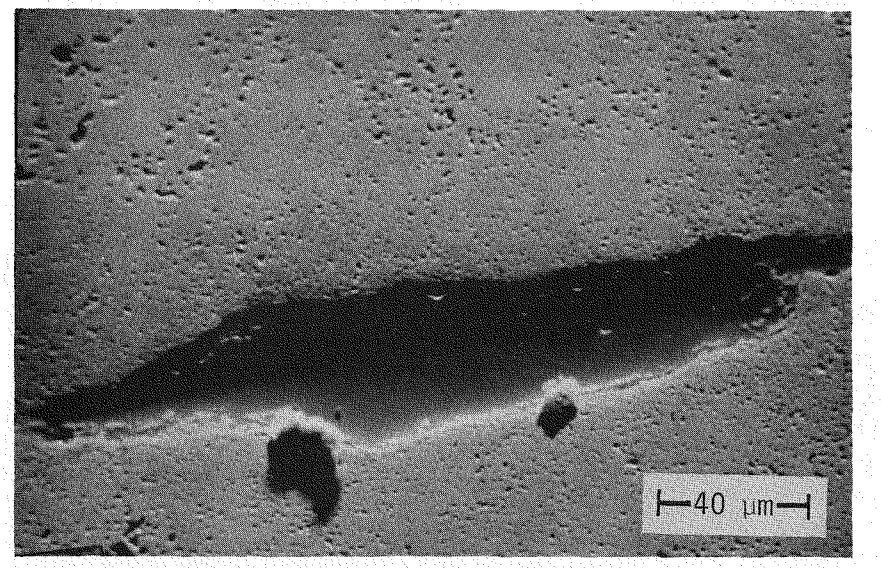

Fe Impurity

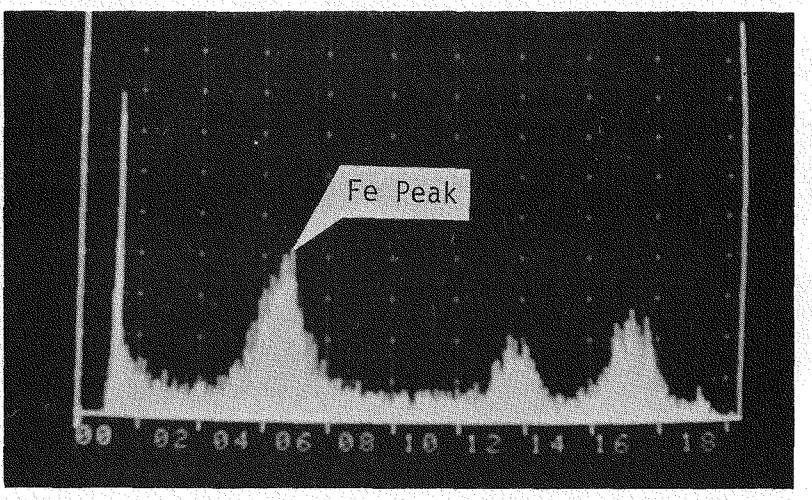

X-Ray Spectrum of Fe Impurity

FIGURE 12. Typical Fe Impurity in Sphere 4

elsewhere in this report). The scale and heterogeneous distribution of the impurities and the nature of the sampling method may prevent chemical analysis of shard samples from detecting iron. To date, no abnormally high Fe concentrations have been detected by chemical analyses of shard samples from spheres made in the PuFF Facility.

Free iron impurities represent a potential threat to vent plugging and compatibility in encapsulated fuel and, thus, should be eliminated. A more gentle sharding process and/or modification of sharding equipment may be necessary.

PARAMETRIC EXPERIMENT IN THE PuFF FACILITY

As described in the January/February report,[1] a statistical parametric study is being applied to the production of shards and hot-pressed pellets in the PuFF Facility to identify some of the product-sensitive variables in the fabrication of MHW spheres. Twenty-six $^{238}PuO_2$ pellets ($\sim$18 g each) have been fabricated and analyses, including metallography, of the pellets are under way.

Statistical analysis of pellet bulk densities revealed that hot press pressure (or load) was the most important process variable for controlling final pellet density, followed by hot press temperature, feed powder particle size, hot press load application rate, and shard sintering temperature. The effect of load application rate appears to depend on die configuration and size and has been shown to be very important for spheres.[2] Analysis of tap densities of presintered shards indicated that feed powder particle size is the process variable which had the strongest influence on shard quality for the milling conditions used.

Description of Parametric Experiment

The objective of the study is to verify or revise the centerline flowsheet for MHW spheres in the PuFF Facility, and establish practical limits on key process variables. The study was designed to evaluate eleven process variables involved in making both shards and hot-pressed fuel forms (Tables 1 and 3) and to determine the sensitivity of the product to these variables. The parametric study ranks the significant variables studied in order of their importance to the property being measured (e.g., pellet density, etc.) and provides information on the practical limits for each variable. Because the results of the study are only valid within the limits chosen for the variables, these limits were selected to bracket the expected centerline value of each process variable. Centerline values or conditions are those given in Table 1 of the November/December 1977 report[4] with the

modified hot pressing conditions previously[2] used for Sphere 13. The limits selected (Tables 1 and 3) were made as broad as practical with the expectation of bracketing the desired fabrication response. Eighteen-gram pellets, rather than full-size spheres, were used to assess hot pressing parameters in order to avoid the large quantity of $^{238}PuO_2$ needed for spheres.

Several characteristics or properties of the $^{238}PuO_2$ pellets and intermediate products are being measured to determine the effects of the key process conditions varied in the parametric experiment. These properties include pellet (bulk) density, shard tap density, powder particle size, and fuel microstructure. This report presents preliminary results of a statistical analysis of data on shard tap density and pellet bulk density.

Tap Densities of Sintered Shards

Shards pre-sintered to a high density should resist break-up during hot pressing better than do shards of a lower density. Fuel made with high-density shards, therefore, should better retain the coarse intershard porosity necessary for dimensional stability of the fuel during final heat treatment. Tap density is related to shard density. Higher tap density implies either higher shard density or better packing because of changes in shard shape or size distribution. To the extent that tap densities reflect shard densities, tap density can be used as an approximate index of sinterability. It should be recognized, however, that such a correlation may be ambiguous because high tap density is also caused by an increase in fines content or compactibility (shape effect).

Analysis of shard tap densities, summarized in Tables 1 and 2, showed that at the 95% confidence level ($\pm 2\sigma$) the only statistically significant variables (of those variables studied within their respective levels) in controlling tap densities were feed powder mode size and mill style (LASL vs. SRL). The relative importance of each variable tested in the preparation of pre-sintered shards is given in the "Significance" column of Table 1. The higher the number, referred to as the "Factor Effect," the more sensitive the response to the variable. The sign of the factor effect indicates which limit leads to an increased response; e.g., if the factor effect is "-", then approaching the lower limit increases the value of the response. The minimum significant factor effect is the minimum absolute value that a factor effect must have to be considered statistically significant at a given confidence level, such as 95% (2σ). The confidence level is a measure of the probability that the differences seen in the responses are a result of the high and low levels of the variables and not the result of normal experimental fluctuations.

TABLE 1

Significance of Parametric Variables

	Variable	*Centerline*	*Variable Levels* +	-	*Significance (Factor Effect)*
X_1	Feed Powder, Particle Mode Size	4-6 μm	6.7 - 8.2	4.2 - 4.3	-0.39
X_2	Mill Style	-	SRL-w/baffle 100 rpm	LASL-w/o baffle 27 rpm	-0.38
X_3	Mill Charge	75 g	80	65	0.04
X_4	Mill Time	12 hr SRP 32 hr LASL	14 hr SPR 32 hr LASL	8 hr SRP 24 hr LASL	0.07
X_5	Post Ball-Mill Screening	300 μm	300 μm	125 μm	0.19
	(Cold Press)	58,000 psi	Constant at 58,000 psi		
X_7[a]	Shard Method	-	Brush Thru	Roll Thru	0.22
X_6[a]	Allow Green Shards to Stand	-	Yes	No	-0.16
X_8	Shard Sinter Temperature	1175°C	1300	1150	0.12
			Minimum Significant Factor Effect = 0.38		

a. These two deliberately reversed

TABLE 2

Shard Tap Densities vs. Fabrication Parameters

Run	*Density, g/cc*	*Total Factor Effect*	*Permutations of Variables* x_1 x_2 x_3 x_4 x_5 x_6 x_7 x_8
9	5.49	0.70	- + - + + - + +
6	5.43	0.59	+ - - - + - + +
12	5.42	0.55	- - - - - - - -
11	5.35	0.43	- + + - + + + -
8	5.31	0.35	- - + - + + - +
10	5.31	0.35	+ - + + - + + +
7	5.28	0.29	- - - + - + + -
2	5.20	0.15	+ - + + + - - -
3	5.14	0.01	- + + + - - - +
4	4.62	-.99	+ + + - - - + -
1	4.60	-1.02	+ + - + + + - -
5	4.50	-1.29	+ + - - - + - +

The only significant factor effects in Table 1 are those given for feed powder size and ball mill style. Feed powder with a mode size of about 4 μm gave significantly higher tap densities than feed powder of mode 6 to 8 μm. Also, LASL-style ball mills gave higher tap densities than do SRL-style mills. Other variables that were not significant at the 95% confidence level, but would have been at, say, the 80% level, were method of sharding (brushing vs. rolling), post-ball mill screen size, and possibly standing of the green shards. Brushing the shards through screens tended to give higher tap densities than rolling them through, as did the use of the coarse post-ball mill screen compared to the finer screen.

The other variables showed small or negligible trends, so that within the limits selected for the test, these process steps appear to have little or no effect on tap density. This is most notable for the ball mill time. The value and sign of its factor effect indicates that milling for longer times had only a small effect on increasing the tap densities and, thus, densities of the shards. This is not to say that ball milling time is not important, but only that there is a small difference between 8 and 14 hr for the SRL mill and 24 and 32 hr for the LASL mill for the range of feed powder tested.

Table 2 lists the fabrication runs in order of decreasing tap density along with the permutations of variable levels for each run. Also in Table 2, the "Total Factor Effect" for each run has been calculated by combining the factor effects of each variable algebraically according to the pattern of variable levels ("+" and "-" refer to high and low levels, respectively) used for that run. Trends in processing can be estimated from the data of Tables 1 and 2. The analysis approximates shard tap density as a linear function of the factor effects. Therefore, it is possible to estimate the tap density arising from combinations of process variables other than those shown in Table 2. To do so, one calculates the total factor effect for the combination of variables to be used, and then interpolates the data in Table 2 to obtain the corresponding tap density. For example, with other factors constant, a combination of small feed size and LASL-style mill produces high tap densities, while a combination of large feed size and SRL-style mill produces low tap densities. Other combinations would result in densities between these extremes. Likewise, brushing the shards through the screens tends to compensate for using large feed powder or an SRL-style mill.

Pellet Density

The shards made with the bilevel process conditions described in Tables 1 and 2 were hot pressed into 18-g pellets. The bilevel process conditions used for the overall parametric design are given in Table 3. The experimental design used tested eleven process variables. Eight variables were used in preparing the shards (Table 1) and three in hot pressing. Those selected for hot pressing were hot-pressing pressure (load), rate of load application, and temperature. The upper and lower levels for these variables were selected on the basis of experience[2] with Spheres 11-15.

TABLE 3

Significance of Parametric Variables; As-Pressed and Hot-Pressed Pellet Density

	Variable	*Experimental Level* +	-	*Significance, % TD* *Factor Effects, As-Pressed Density*	*Factor Effects, Heat-Treated Density*
1	Feed Size, μm	6.7-8.2	4.2-4.3	0.8	1.1
2	Mill Style	SRL	LASL	0	0.0
3	Mill Charge, g	80	65	-0.1	0.4
4	Mill Time, hr SRP LASL	14 32	8 24	0.7	0.6
5	Post Ball-Mill Screen Size, μm	300	125	0.5	0.5
6	Store Green Shards	Yes	No	0.9	0.4
7	Shard Method	Brush	Roll	0.8	0.5
8	Shard Sinter Temperature °C	1300	1150	1.2	0.4
9	H.P. Pressure psi	2950	875	2.3	2.6
10	Press Rate, sec[a]	10	180	0.6	0.9
11	H.P. Temperature, °C	1550	1450	1.9	1.0
	Minimum Significant Factor Effect @ 95% Confidence Level			1.2	1.2

a. Time from initiation of pressing load ramp to final load or pressure.

The analytical results are summarized in Table 3, which gives the factor effects of each of the shard fabrication and hot-pressing variables for the bulk densities of both as-pressed and final heat-treated pellets. At a 95% (2σ) confidence level, the minimum significant factor effect is 1.2% TD. Therefore, for as-pressed pellets the statistically significant variables were pressing pressure, hot press temperature, and shard sintering temperature. For heat-treated pellets, only hot pressing pressure was statistically significant. The factor effects for several other variables (e.g., hot press temperature, feed powder size and pressure application rate), even though numerically less significant, probably correctly reflect the trends indicated by their signs.

Tables 4 and 5 list, respectively, in descending order, the densities of as-pressed and final heat-treated pellets with the corresponding total factor effects and the permutations of the seven highest ranking variables for each run. Data in Table 5 indicate that hot press pressures lower than the 3000 psi used for Spheres 1-10 are essential in order to achieve densities in the 80-82% TD range desired. As indicated above for shards, the factor effects can be combined to roughly estimate pellet densities for different combinations of variables.

It is important to know whether or not combinations of variables that give equivalent densities (e.g., Runs 1, 3, 10 in Table 5) also give equivalent macro- and microstructures. Therefore, metallography is in progress to compare porosity, grain size, cracking, and suboxide formation.

TABLE 4

As-Pressed Pellet Density vs. Fabrication Parameters

Run	*Density, % TD*	*Total Factor Effect, % TD*	*Permutations of Variables* x_1	x_4	x_7	x_8	x_9	x_{10}	x_{11}
7	86.0	4.3	-	+	+	-	+	+	+
5	85.6	4.1	+	-	-	+	+	-	+
2	83.7	3.1	+	+	-	-	+	-	+
6	83.0	2.3	+	-	+	+	-	+	+
8	82.4	-.1	-	-	-	+	+	+	-
9	82.4	1.7	-	+	+	+	+	-	-
3	80.2	0.5	-	+	-	+	-	+	+
4	80.1	0.7	+	-	+	-	+	+	-
10	80.0	-1.3	+	+	+	+	-	-	-
11	79.3	-2.9	-	-	+	-	-	-	+
1	78.4	-4.1	+	+	-	-	-	+	-
12	71.5	-8.3	-	-	-	-	-	-	-

TABLE 5

Heat-Treated Pellet Density vs. Fabrication Parameters

Run	*Density, % TD*	*Total Factor Effect, % TD*	*Permutations of Variables* x_1	x_4	x_7	x_8	x_9	x_{10}	x_{11}
7	86.6	4.1	-	+	+	-	+	+	+
2	∿86[a]	3.5	+	+	-	-	+	-	+
5	85.6	3.1	+	-	-	+	+	-	+
4	85.6	3.1	+	-	+	-	+	+	-
9	83.7	1.1	-	+	+	+	+	-	-
8	84.9	0.7	-	-	-	+	+	+	-
6	83.5	0.7	+	-	+	+	-	+	+
3	81.1	-1.3	-	+	-	+	-	+	+
1	81.5	-1.9	+	+	-	-	-	+	-
10	81.2	-1.9	+	+	+	+	-	-	-
11	80.2	-4.1	-	-	+	-	-	-	+
12	74.6	-7.1	-	-	-	-	-	-	-

a. The pellet was dropped and broken before its bulk density was measured. The density shown is estimated from Factor Effects.

TABLE 6

Effects of Combinations of Significant Variables

Variable	*Factor Effect, % TD*		*Approx. Worth per 1% Δ Density*
	As Pressed	*Heat Treated*	
Hot press pressure	2.3	2.6	400 psi
Hot press temperature	1.9	1.0	50°C
Feed powder mode size	0.8	1.1	1.5 μm
Press load application rate	0.6	0.9	*a*
Shard sintering temperature	1.2	0.4	87°C[b]
Minimum significant factor effect, 1.2% TD			

a. Not calculable
b. Calculated using average of as-pressed and heat-treated Factor Effects.

Interpretation of Density Analyses

The most significant variables are ranked in order of importance in Table 6. Only those factor effects which exceed the range of experimental error (2σ) give a reliable indication of the sign and magnitude of the response to a variation in a given process condition. The smaller the factor effect reported in Tables 3 and 6, the more uncertain are its magnitude and sign, because the probability of having a chance experimental fluctuation of that sign and magnitude increases proportionately.

For the heat-treated pellets the only factor effect exceeding 2σ was the one for hot press pressure. However, the indicated effects for the other variables listed in Table 6 are probably also meaningful because of their relative magnitudes (approaching 2σ) and the consistency of their signs for as-pressed and heat-treated pellets.

In arriving at the ranking of Table 6, factor effects from both the as-pressed and heat-treated densities were considered jointly with more weight being given to the heat-treated factors. Within the limits tested, the order is also expected to apply to MHW spheres with the exception of pressure application rate, which is known from work with Spheres 11-15 to be strongly geometry- and size-sensitive. On the basis of past experience, pressure application rate is expected to rank at least third and perhaps even second. The last column of Table 6 indicates the approximate change in magnitude of a variable necessary to effect a 1% change in relative density of the pellets as determined by statistical analysis of the bulk densities.

As expected[1] hot press pressure had the most significant effect on pellet density of any variables, confirming the results[2] of Spheres 11-13. Table 5, Column X_9, shows that in order to obtain densities in the desired range of 80 to 82% TD, hot press pressure significantly less than 3000 psi is necessary. The optimum pressure cannot be deduced from these experiments, but it is probably close to the lower pressing limit.

Hot press temperature did not have as much effect on pellet densities as did hot press pressure, again confirming earlier expectations.[1] Load application rate did not have as strong an effect as anticipated, based on Spheres 11-15, indicating pressure application rate is strongly dependent on size and geometry. As indicated recently,[2] load application rate is very important in fabrication of spheres. As expected, some important variables have interaction effects which may mask their individual significance. This may be true of hot press temperature and pressure application rate.

The factor effect for feed powder mode size was negative in the tap density analysis but was positive in the analysis of pellet density. This substantiates observations in earlier SRL work[5,6] and reflects the effect of particle size on shard density and of shard density on pellet density. Larger particles do not mill as fine in the time range given as do small particles; consequently, they product less-dense, more-sinterable shards which in turn lead to higher pellet densities.

The effect of shard sintering temperature on pellet density was smaller than expected from Sphere 3 results (described earlier) and was also opposite in sign to the expected response. As described above, shards of higher density are expected to consolidate into fuel of lower density, which is opposite to the shard sintering effects realized for both the as-pressed and heat-treated pellets. Perhaps the increase of shard density and integrity for an increase in presintering temperature from 1150 to 1300°C was obscured during hot pressing. This would suggest that shards for Sphere 3 were pre-sintered at higher temperatures than indicated, or that the combination of powder and sharding conditions during Sphere 3 fabrication led to shards of significantly higher density than shards sintered at 1300°C during the parametric experiment. On the other hand, the tap density data suggest there may have been very little change in shard density between the two sintering temperature levels used in the parametric study. Thus, the effect may truly have no significance. Analyses of the microstructures of the shards and pellets may explain this apparently anomalous effect.

Several of the less-significant variables are of interest because they were expected to be important and were not. The ball mill-type which was analyzed to be the second most important variable to shard tap densities was not significant to the density

of hot-pressed pellets. This suggests the high tap density was probably due to some morphological property of the LASL-milled material that was completely obscured during hot pressing.

Variation in mill charge within the range selected was also insignificant. The small effect of milling time indicates that the changes in powder size during the milling interval selected (8 vs. 14 hr for SRL mill) did not significantly affect final fuel density.

Other variables involved in the powder and sharding operations which affect shard morphology and density did not test to be significant in controlling final fuel density. However, these variables, if allowed to vary excessively and through synergistic interactions, could affect the product.

Conclusions

Several preliminary conclusions can be drawn from analysis of the density data: (1) much lower hot pressing pressures (∿1500 psi) than specified in the original flowsheet are essential for successful sphere fabrication; (2) variations in feed size (or milled powder size) noticeably affect the process; and (3) the SRL design ball mill can be used since the two mill styles (SRL and LASL) gave essentially equivalent results. Final recommendations will be made following metallographic analyses of the parametric pellets and full-scale verification of the pellet results with MHW spheres.

HEAT TRANSFER IN $^{238}PuO_2$ SPHERE SHIPPING PACKAGE

Encapsulated $^{238}PuO_2$ spheres will be shipped from SRP in shipping casks designed to hold four spheres welded in individual primary shipping cans (Figure 13). Heat transfer analysis was performed on the expected shipping arrangement to supply information for the Safety Analysis Report - Packaging and to allow selection of appropriate sphere packing material inside the primary shipping container to assure that the sphere center temperature does not exceed 800°C. As a result of this analysis, graphite felt, the original candidate for sphere packing material, was replaced with solid graphite blocks. Decreasing the gap between the primary and secondary shipping containers and changing the gas in this gap was also investigated. These changes did not improve heat transfer sufficiently to decrease the sphere temperatures below acceptable limits without the replacement of the graphite felt with solid graphite blocks.

Physical Description

A schematic drawing of a $^{238}PuO_2$ sphere in its primary container is shown in Figure 14. The iridium shell is 0.024 in. thick and is separated from the $^{238}PuO_2$ sphere by a 0.085-in., helium-filled gap. The primary container is a 0.085-in.,, filled with helium, and four such containers are to be stacked in a cylindrical secondary container. The secondary container, in turn, is placed inside the PISA shipping cask in the manner shown in Figure 13.

Original plans called for supporting the $^{238}PuO_2$ spheres against shock within their primary containers with RVG 4000r* graphite felt as shown in Figure 14. Each $^{238}PuO_2$ sphere releases 100 to 103 watts of power.

Heat Transfer Through Primary — Secondary Container Gap

The center temperature of the $^{238}PuO_2$ sphere may be affected by changing the gap thickness or interstitial gas in the gap between the primary and secondary containers. Air and helium were considered over a range of radial gap thicknesses from 0.010 to 0.045 in. Shipping specifications call for a maximum radial gap of 0.045 in. and for air within the gap.

* Product of Fiber Materials, Inc., Biddeford, Maine.

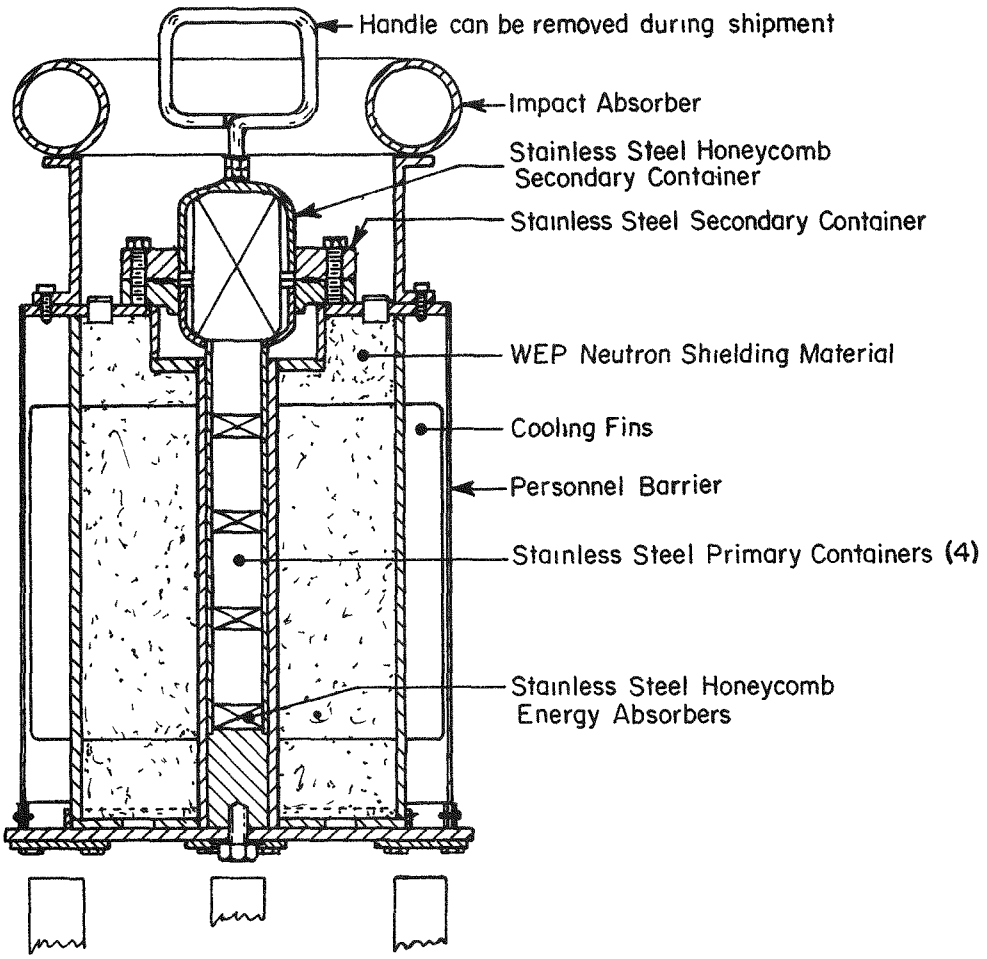

FIGURE 13. Post-Impact Sphere Assembly (PISA) Shipping Cask Assembly

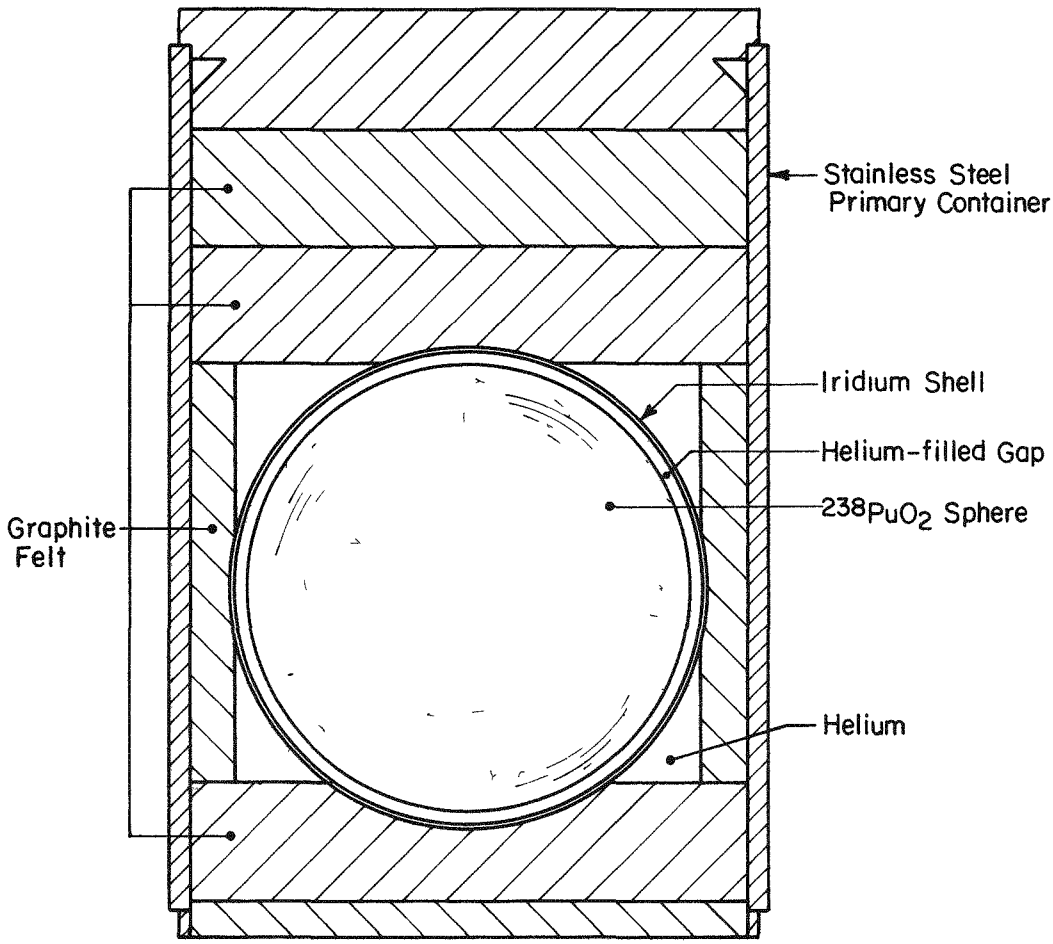

FIGURE 14. Primary Container for $^{238}PuO_2$ Sphere

Congestion and axial heat transfer were assumed to be negligible. Therefore, the applicable equation for heat transfer is,

$$Q \simeq Q_{conduction} + Q_{radiation}$$

$$Q \simeq \frac{K_{gas}\, 2\pi L(T_o - T_i)}{\ln r_o/r_i} + \frac{0.1714 \times 10^{-8} A\, (T_o^4 - Ti^4)}{\frac{1}{\varepsilon_i} \quad \frac{r_i}{r_o} \quad \frac{1}{\varepsilon_o - 1}}$$

where

Q = heat transfer, Btu/hr

k_{gas} = thermal conductivity of interstitial gas, Btu/hr ft °F

L = length over which heat transfer occurs, 0.208 ft

r = radius, ft

T = temperature, °R

A = surface area through which heat is transferred, ft^2

ε = emissivity (0.6 assumed),

and the subscripts are

i = inner wall surface of secondary container

0 = outer wall surface of primary container.

For assumed values of T_i, increasing values of T_o were chosen, and the heat transfer was computed. A solution was found when a value of T_o corresponding to a heat transfer of 103 watts was determined. Solutions were obtained for a range of secondary inner surface temperatures (T_i).

Results are given in Figure 15. Previous measurements on a full-scale mockup of the entire PISA shipping cask indicated an average temperature difference of 301°F across an air-filled, 0.027-in. gap for T_o = 234°F. For these same conditions, Figure 15 gives a conservative estimate of 325°F for a +6° error. As would be expected, the results for helium indicate significantly smaller temperature differences.

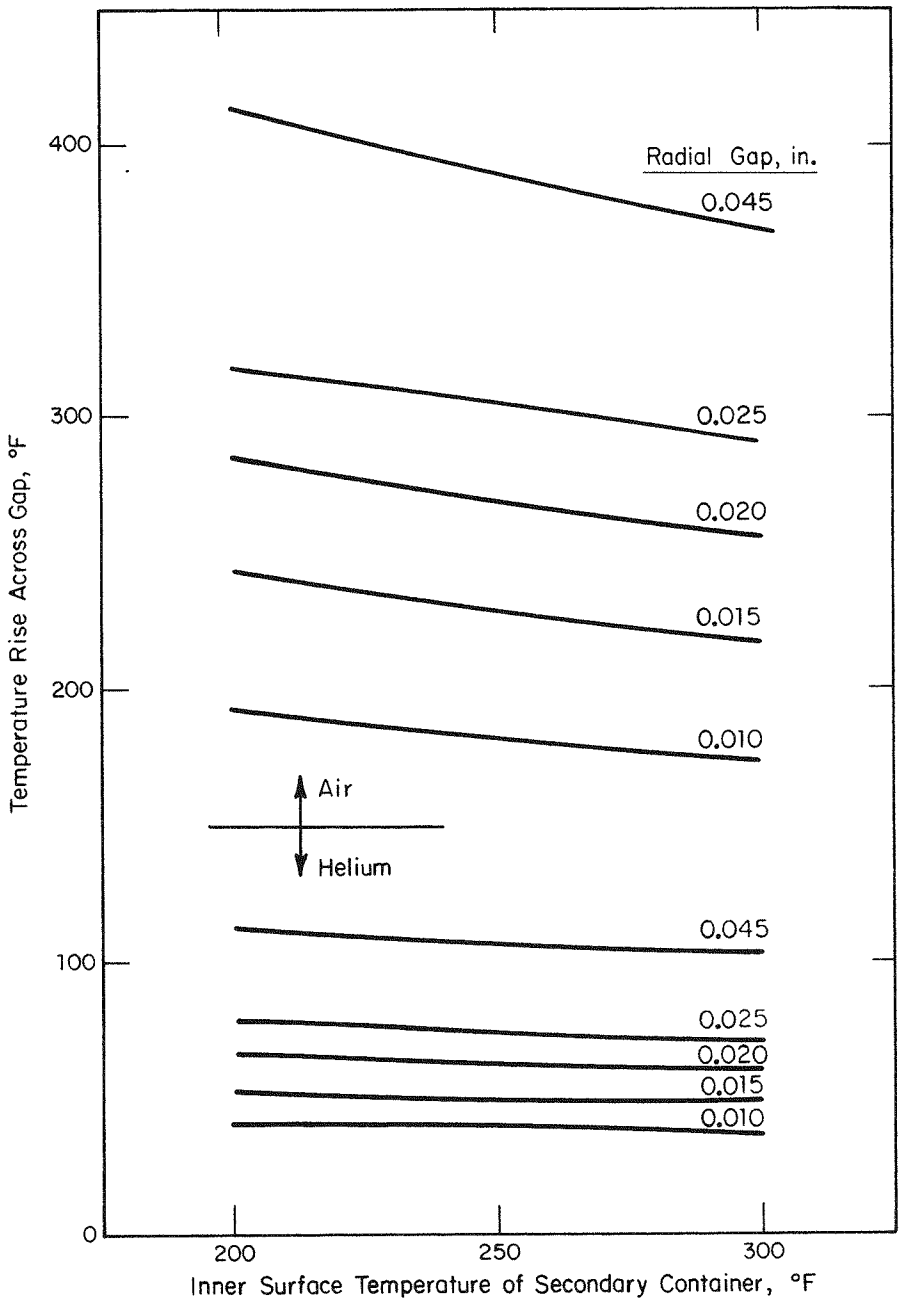

FIGURE 15. Temperature Rise Across Primary-to-Secondary Container Gap for PISA Cask

Heat Transfer Between Primary Container and Sphere Center

Three primary container packaging configurations were considered: 1) graphite felt (shown in Figures 13 and 14),[2] solid graphite filler throughout the entire primary container cavity surrounding the $^{238}PuO_2$ sphere, and 3) a partial solid graphite support as shown in Figure 16. The first case models the shipping package as planned at the time this study was initiated. The second is a hypothetical case designed to determine the maximum benefit from use of solid graphite to reduce sphere center temperatures. The third is a modification suggested by PuFF personnel.

The following assumptions were made:

1. No heat is transferred from the end of the primary container. This assumption is correct for the central container in a stack but is conservative for the end containers.

2. Both radiation and convection heat transfer modes have negligible contributions. This assumption is conservative.

3. The thermal conductivities for stainless steel and solid graphite (AXM-50) are constant. Since their values are relatively large anyway, small changes in conductivity over the temperature range involved have little effect on the ultimate temperature distribution.

4. The temperature rise across the shell can be neglected because the conductivity of the iridium shell is very high and its thickness is very small.

5. The thermal conductivity of the RVG 4000 graphite felt is the same as for helium because its void fraction is over 99%. The manufacturer's literature supports this assumption.

6. Heat generation within the $^{238}PuO_2$ sphere is uniform.

By symmetry, the physical configuration reduces to a three-dimensional axisymmetric problem. The steady-state temperature distribution is given by Fourier's law of heat conduction.

$$\frac{\partial}{\partial r}\left(Kr\,\frac{\partial T}{\partial r}\right) + \frac{\partial}{\partial z}\left(Kr\,\frac{\partial T}{\partial z}\right) + rQ = 0$$

with the boundary conditions,

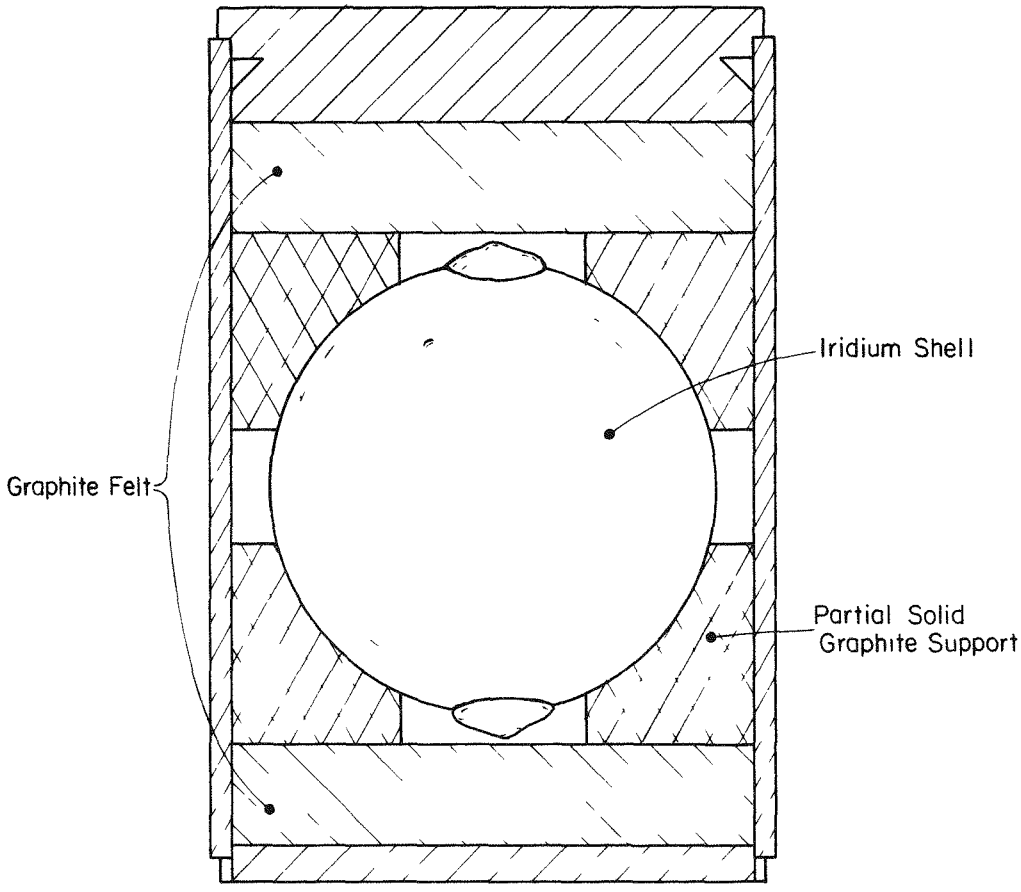

FIGURE 16. Primary Container with Partial Graphite Support

T = constant on the primary container wall surface and

$\frac{dT}{dN}$ = 0 (no heat transfer) on all other boundaries.

Although this equation may be solved by a number of means, the complexity of the geometry involved (a sphere in a cylinder) suggested a solution by the method of finite elements. Finite elements are more easily applied to irregular boundaries than are finite difference techniques or classical analysis.

A computer program written by Huebner[7] was used. The program provides for thermal conductivity changes between elements; however, no allowance is made for property changes with temperature. Therefore an iterative approach was taken whereby thermal properties were updated until the temperature and property distributions were compatible.

For materials with well-established thermal properties such as helium and steel, this iterative procedure poses no problem. Unfortunately, the thermal conductivity for $^{238}PuO_2$ spheres is not so well established. Figure 17 shows thermal conductivity for $^{238}PuO_2$ spheres as a function of temperature. The data are divided into two groups: one is directly proportional to temperature and the other is inversely proportional to temperature. All data appear to converge at higher temperatures. Mellen[8] indicates that the "inverse" behavior would be expected for ceramics above their Debye temperature. Kent and Zocher[9] attribute the "direct" behavior to helium trapped within the microstructure of the spheres. Of the five data sets represented, none could be distinguished as being accurate. Therefore, values for thermal conductivity directly proportional to temperature (the lower values) were used in this study as a conservative measure.

Results of calculations for $^{238}PuO_2$ sphere center temperatures are given in Figure 18. The curves show that use of RVG 4000 graphite felt would result in sphere center temperatures above 800°C regardless of any practical modifications that might be made in the primary-to-secondary gap. On the other hand, use of the solid graphite filler would always result in sphere center temperatures below 800°C. However, a solid graphite filler is not a practical alternative since it would provide no shock absorption qualities.

PuFF personnel have suggested a compromise that incorporates a tightening of the primary-to-secondary gap specifications to allow only a 0.036-in. maximum and installation of the partial solid graphite support. If a secondary container wall temperature of 235°F with air in the gap is assumed, these modifications should result in a primary container wall temperature less than 650°F and a $^{238}PuO_2$ center temperature of less than 750°C.

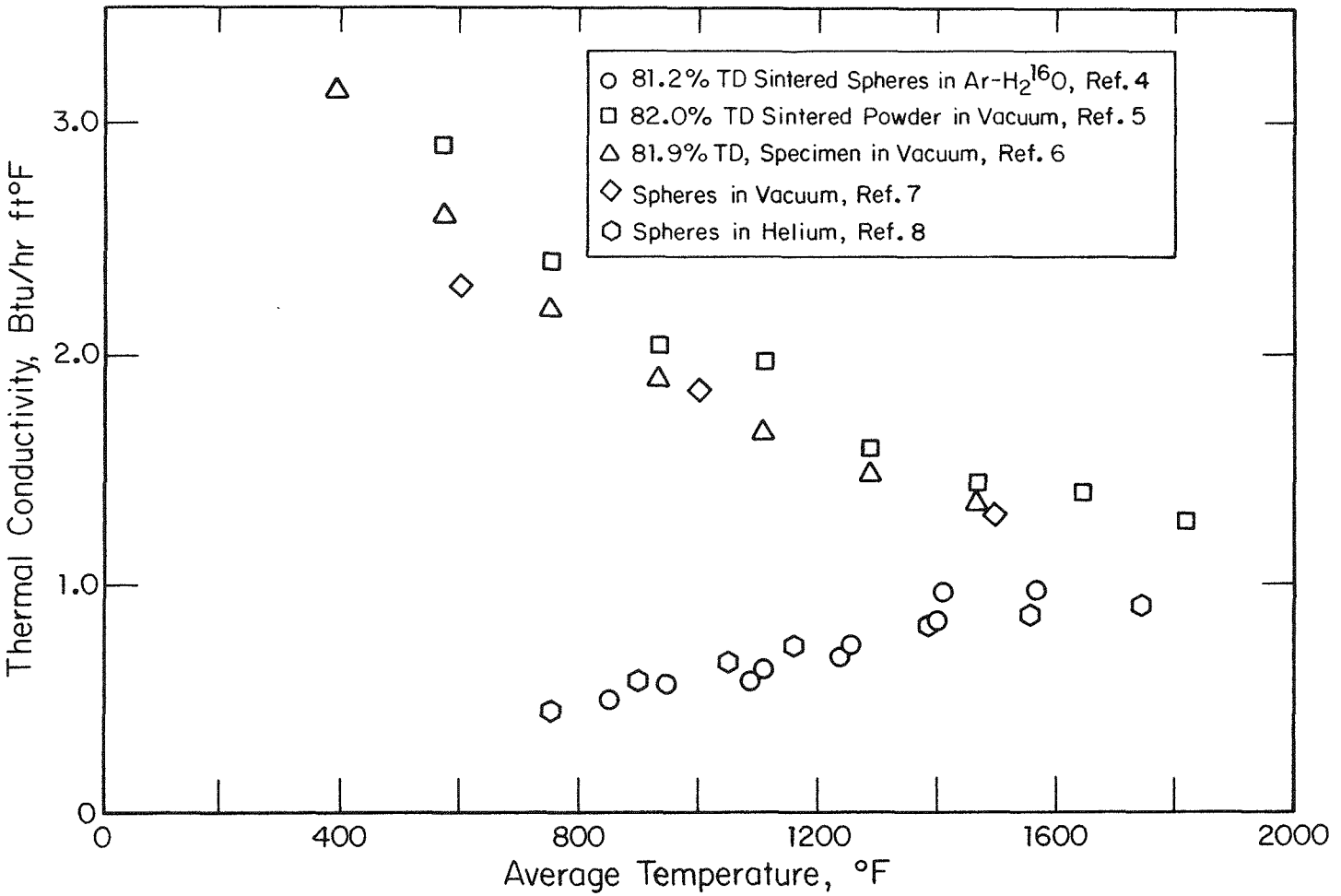

FIGURE 17. Thermal Conductivity of $^{238}PuO_2$ Spheres

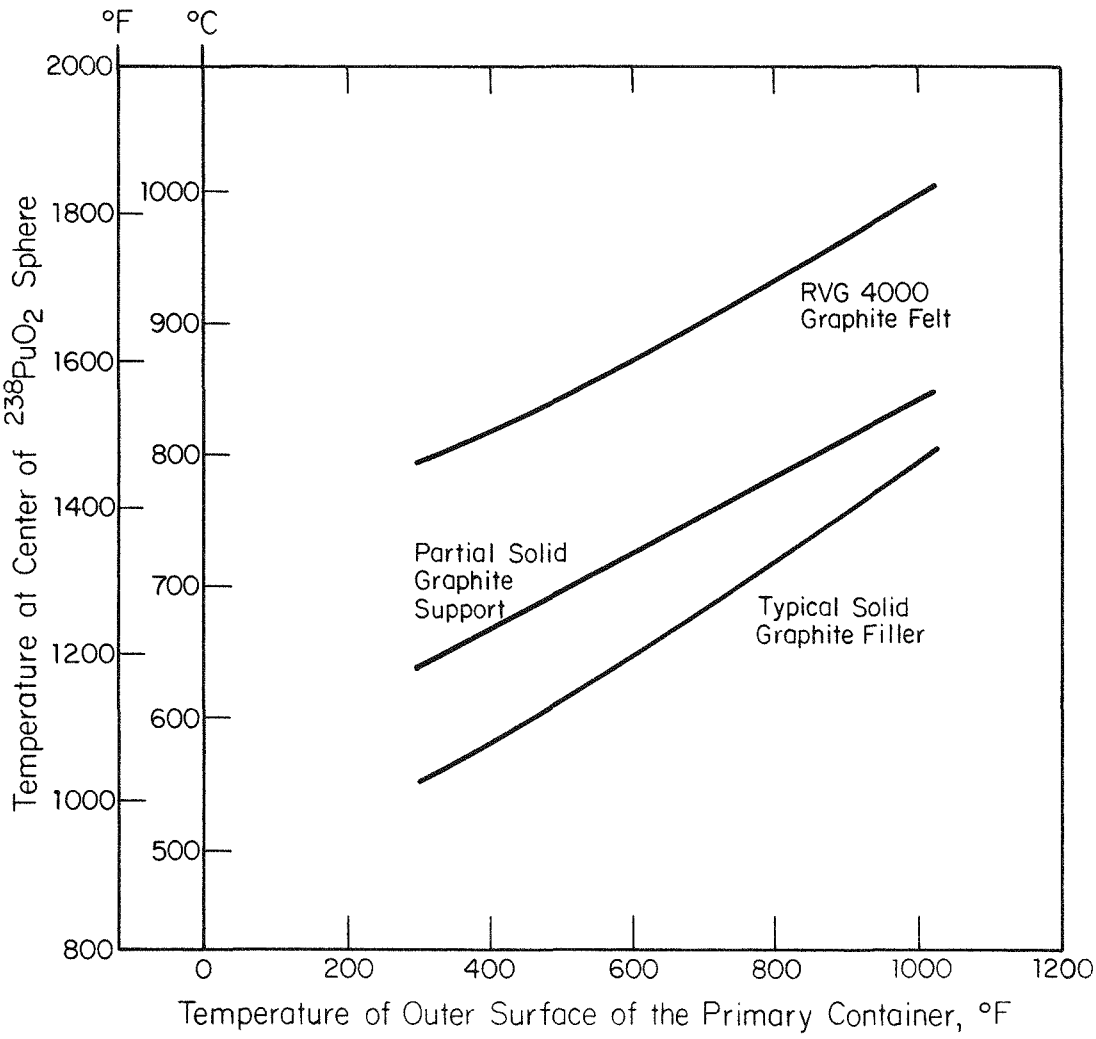

FIGURE 18. Center Temperatures for $^{236}PuO_2$ Spheres in Primary Containers

PROCESS DEVELOPMENT FOR SPACE APPLICATIONS

MICROSTRUCTURAL EFFECTS OF REDUCING ATMOSPHERES ON AGED $^{238}PuO_2$ PELLETS

Preliminary investigation revealed no definitive effect of hydrogen atmospheres on microstructural damage produced by helium agglomeration in $^{238}PuO_2$ pellets aged at 1100°C. The hypothesis that phase changes accompanying reduction and subsequent reoxidation might allow escape of helium with less damage to the fuel was not borne out by experimental observation. However, absence of substoichiometric phases in the microstructure indicated that this heat treatment temperature may have been too low for substantial reduction of the $^{238}PuO_2$ pellets. A notable result of the study was the observation of microcracking in as-pressed $^{238}PuO_2$ pellets, which had not been heat treated to reoxidize the substoichiometric structure prior to long-term aging; this microcracking was attributed to internal stresses produced by reoxidation at low temperatures during aging of the pellets.

The specimens employed in the test were segments of two 1/4-in.-diameter by 1/4-in.-thick $^{238}PuO_2$ pellets prepared in March and April 1975 and stored for 30-32 months near room temperature in air.[10] Both pellets were fabricated from ∿125-μm oxalate-base $^{238}PuO_2$ shards by hot pressing in a multicavity graphite die under 3000 psi pressure for 20 min at 1530°C in vacuum atmosphere. One pellet (MPH 41-5) was heat treated at 1440°C for 12 hr in air, to oxidize the substoichiometric as-pressed structure to $^{238}PuO_2$, while the second pellet (MPH 40-1) was stored in the as-pressed (not heat-treated) condition. Density of the first pellet was 78.3% TD as pressed and 80.4% after heat treatment, and the density of the second pellet was 77.9% TD as pressed. Typical microstructure displayed high-density regions representing the original shards surrounded by large irregular pores (July 1975 report,[11] p 14). Grain size in the high-density regions was <15 μm.

After storage, the pellets were sectioned into several segments, and the segments were heat treated for 4 hr at 1100°C in various combinations of 4% hydrogen/helium and air atmospheres, as given in Table 7. The heat treatment temperature chosen (1100°C) was just below the 1200°C threshold observed previously for formation of well-defined grain-boundary gas bubbles and separations in aged $^{238}PuO_2$ pellets (January/February 1978 Report,[1] p. 52.)

TABLE 7

Atmosphere Conditions for Heat Treatment of $^{238}PuO_2$ Pellet Segments After Aging

Specimen No.	*Heat Treatment Atmosphere*[a]
41-5A	No Heat Treatment
B	4% H_2/He (1 hr) - air (3 hr)
C	4% H_2/He[b]
D	Air
40-1A	No Heat Treatment
B	4% H_2/He (1 hr) - Air (3 hr)
C	4% H_2/He[b]
D	Air

a. All heat treatments at 1100°C for 4 hr.

b. Cooled to 54°C in H_2/He atmosphere before exposure to air.

Microstructures of the specimens after a short (30-min) grain-boundary etch, shown in Figures 19 and 20, revealed no well-defined effect of the reducing atmospheres on the extent of microstructural damage produced by accumulated helium. Several of the specimens showed grain-boundary separations and/or microcracks after the heat treatment at subthreshold (1100°C) temperatures, but the effect was not aggravated in hydrogen atmospheres. No evidence of substiochiometric phases was detected in the hydrogen-treated specimens after a sub-stoichiometry etch, indicating the 1100°C heat treatment temperature may have been too low to produce a substantial reduction of the $^{238}PuO_2$ specimens. The microstructural damage observed in the previously heat-treated specimen was attributed to the usual agglomeration of helium into grain boundaries, at somewhat lower temperatures than previously observed because of minor variations in heat treatment procedures.

The grain separations of microcracks in the as-pressed pellet were observed in specimens not heat treated, as well as in specimens heat treated, after aging. The microcracks in the specimens not heat treated after aging, like grain separations produced by helium agglomerations in heat-treated specimens, were localized within the high-density regions and produced no general fracture of the specimen, unlike the helium-induced grain separations however, they sometimes extended to the edges of the high-density regions. These micro-cracks, which could not be caused by helium at such low temperatures, were attributed

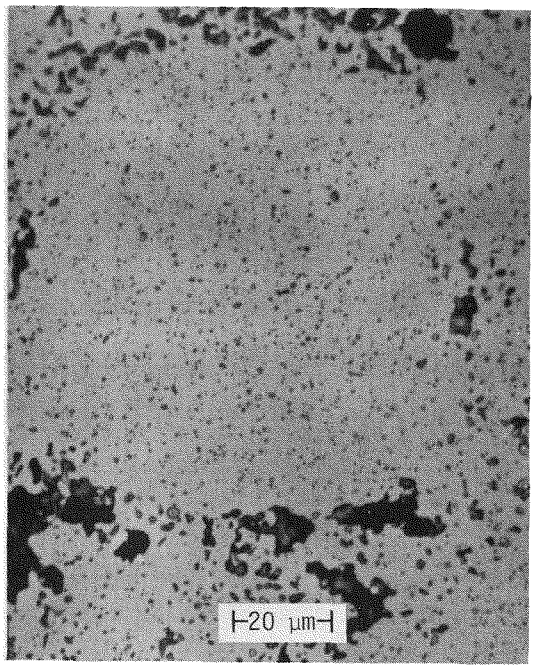

a. Not Heated

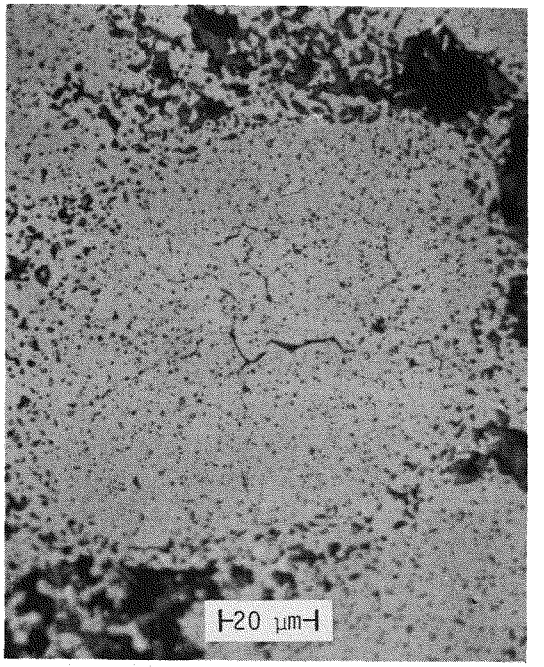

b. Heated 3 hr in 4% H_2/He, 1 hr in Air

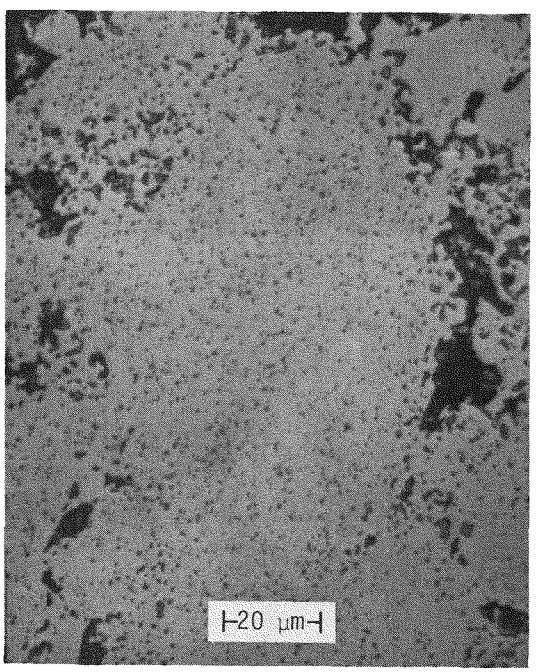

c. Heated 4 hr in 4% H_2/He

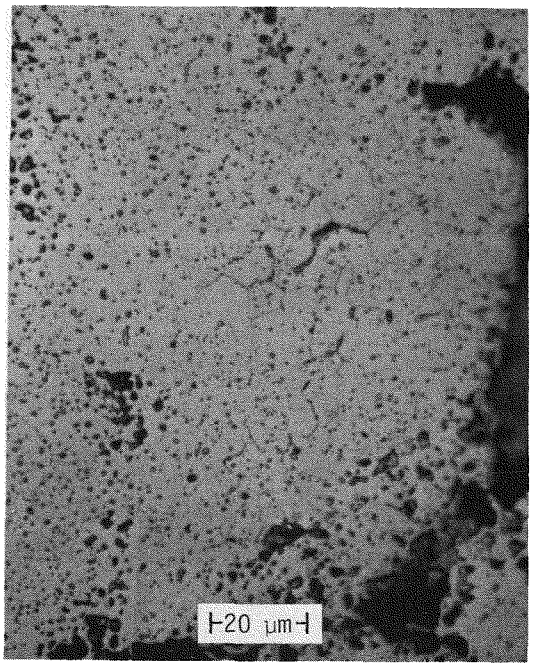

d. Heated 4 hr in air

FIGURE 19 Microstructures of Heat-Treated 80%-Dense $^{238}PuO_2$ Pellet MHP 41-5 Heated at 1100°C in Reducing and Reoxidizing Atmospheres after 32-mo Aging (Etched 30 min)

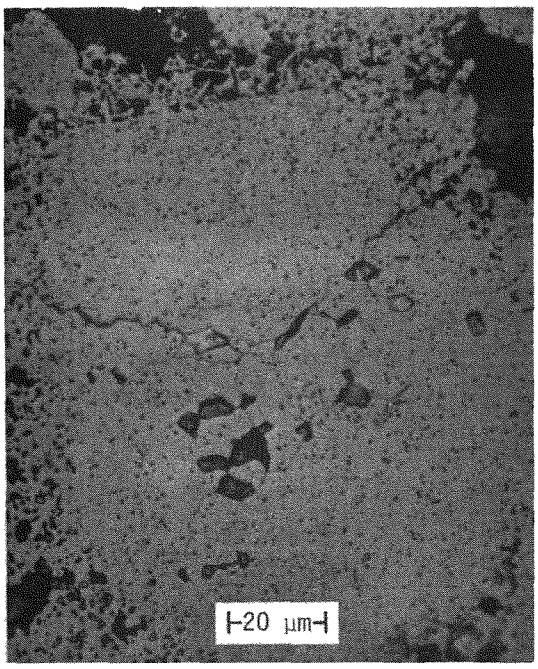

a. Not Heated

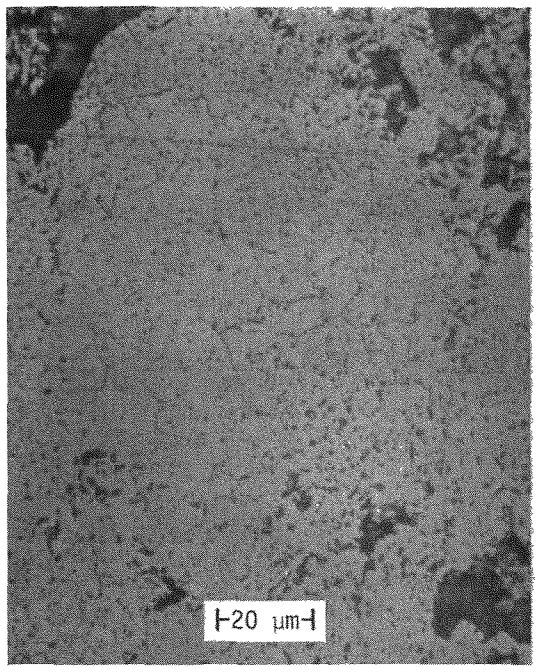

b. Heated 3 hr in 4% H_2/He, 1 hr in Air

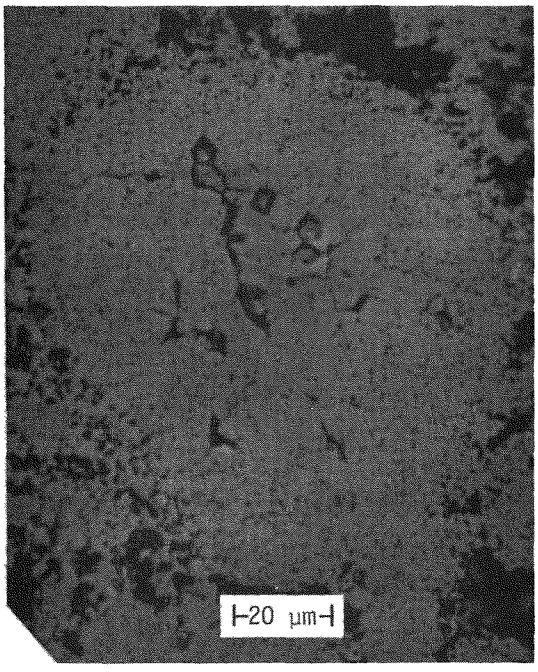

c. Heated 4 hr in 4% H_2/He

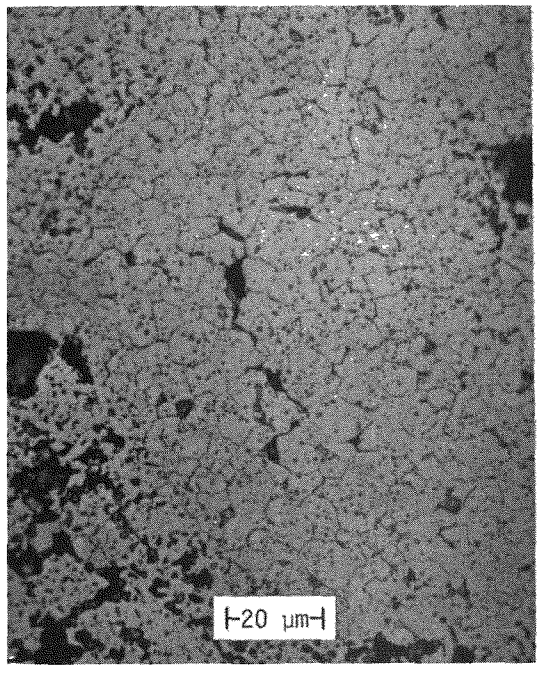

d. Heated 4 hr in Air

FIGURE 20. Microstructures of As-Pressed, 80%-Dense $^{238}PuO_2$ Pellet MHP 40-1 Heated at 1100°C in Reducing and Reoxidizing Atmospheres After 32-mo Aging (Etched 30 min)

tures, were attributed to internal stresses produced by slow reoxidation of the as-pressed specimen during aging at low temperature. Metallographic examination after substoichiometric etching revealed no evidence of substoichiometric phases in the aged specimens.

Definitive effects of heat treating the as-pressed specimens after aging were obscured by the microcracks found before heating. Heating changed the character of the microcracks; they appeared less severe in the heat-treated specimens and did not extend to the edges of the high-density regions of the microstructure. The microcracks in the unheated specimen may thus have sintered somewhat in the heated specimen, with helium depletion at the edges of the high-density regions allowing more complete sintering than in the center of these regions. No definitive effect of the heating atmosphere on the degree of resintering was apparent.

EXPERIMENTAL FACILITIES

PLUTONIUM EXPERIMENTAL FACILITY

Operations with PuO_2 were started in the PEF in early May. Approximately 300 g of $^{238}PuO_2$ feed powder were charged into the glove box line for future MHW sphere fabrication tests, which will begin following completion of simulation testing of the hot press.

In mid-May about 260 g of cold pressed and presintered $^{238}PuO_2$ compacts were received from the PuFF Facility for the special fabrication of prototypic shard fuel for the Milliwatt Program. The remaining steps in the SRL oxalate-base process were completed in PEF, and the finished shards were returned to the PuFF Facility in HB-Line primary containers for preparations to ship them to Mound Laboratory (ML). Fabrication results will be given in the next report.

Simulation tests of the hot press with ThO_2 were further delayed by two occurrences. First, a water leak developed in one of the water-cooled clamping rams. Three weeks were required to locate the leak, remove the defective ram, and fabricate and install a replacement. Second, one of the heat shields from the PEF press was loaned to the PuFF Facility to permit continued operation of their press. An additional delay of about two weeks was incurred.

Immediate plans are to complete simulation tests of the hot press in July. Concurrently, PuO_2 will be processed to make shards for a test MHW sphere.

REFERENCES

1. *Savannah River Laboratory Monthly Report, ^{238}Pu Fuel Form Processes, January/February 1978.* USDOE Report DPST-78-128-1/2, E. I. du Pont de Nemours & Company, Savannah River Laboratory, Aiken, SC (1978).

2. *Savannah River Laboratory Monthly Report, ^{238}Pu Fuel Form Processes, March/April 1978.* USDOE Report DPST-78-128-3/4, E. I. du Pont de Nemours & Company, Savannah River Laboratory, Aiken, SC (1978).

3. *Savannah River Laboratory Monthly Report, ^{238}Pu Fuel Form Processes, September 1977.* USDOE Report DPST-77-128-9, E. I. du Pont de Nemours & Company, Savannah River Laboratory, Aiken, SC (1977).

4. *Savannah River Laboratory Monthly Report, ^{238}Pu Fuel Form Processes, November/December 1977.* USDOE Report DPST-77-128-11/12, E. I. du Pont de Nemours & Company, Savannah River Laboratory, Aiken, SC (1977).

5. *Savannah River Laboratory Monthly Report, ^{238}Pu Fuel Form Processes, March 1976.* USERDA Report DPST-76-128-3, E. I. du Pont de Nemours & Company, Savannah River Laboratory, Aiken, SC (1976).

6. P. K. Smith, D. F. Bickford, and D. N. Rankin. "Reproducible Fabrication of PuO_2 Fuel." *Mater. Res. Bull.*, 589 (1977).

7. K. H. Huebner. *The Finite Element Method for Engineers,* Wiley, NY (1975).

8. J. B. Mellen. *Heat Transfer in $^{238}PuO_2$ Fuel Spheres.* USERDA Report DP-1433, E. I. Du Pont de Nemours & Company, Savannah River Laboratory, Aiken, SC (1976).

9. R. A. Kent and R. W. Zocher. *Heat Transfer in $^{238}PuO_2$ Spheres.* USERDA Report LA-6340-MS, Los Alamos Scientific Laboratory, NM (1976).

10. *Savannah River Laboratory Monthly Report, ^{238}Pu Fuel Form Processes, April 1975.* USAEC Report DPST-75-128-4, E. I. du Pont de Nemours & Company, Savannah River Laboratory, Aiken, SC (1975).

11. *Savannah River Laboratory Monthly Report, ^{238}Pu Fuel Form Processes, July 1975.* USERDA Report DPST-75-128-7, E. I. du Pont de Nemours & Company, Savannah Riber Laboratory, Aiken, SC (1975).

DISTRIBUTION

Copy No.

1 T. A. Dillon, Acting Director, Advanced Systems and Materials Production Division, U. S. Department of Energy

2 B. J. Rock, Acting Assistant Director, Office of Space and Terrestrial Systems, Advanced Systems and Materials Production Division, U. S. Department of Energy

3 J. J. Lombardo, Acting Chief, Power Systems Branch, Advanced Systems and Materials Production Division, U. S. Department of Energy

4 N. R. Thielke, Acting Chief, Technology Development Branch, Advanced Systems and Materials Production Division, U. S. Department of Energy

5 T. J. Dobry, Acting Chief, Safety and Isotope Fuels Branch, Advanced Systems and Materials Production Division, U. S. Department of Energy

6 R. F. Caudle, Asst. Secretary for Defense Programs, U. S. Department of Energy

7 V. C. Vespe, Albuquerque Operations Office

8 D. K. Nowlin, Albuquerque Operations Office

9 J. A. Chacon, Manager, Dayton Area Office

10 R. D. Baker, CMB, DO, Los Alamos Scientific Laboratory

11 S. E. Bronisz, CMB-5, MS-730, Los Alamos Scientific Laboratory

12 R. A. Kent, Los Alamos Scientific Laboratory

13 W. T. Cave, Monsanto Research Corporation

14 B. R. Kokenge, Monsanto Research Corporation

15 Technical Library, Sandia Laboratory, Albuquerque

16 M. K. Parson, Sandia Laboratory, Albuquerque

17 T. J. Young, Sandia Laboratory, Albuquerque

18 E. W. Williams, General Electric Company, Philadelphia

19 N. B. Elsner, Gulf General Atomic, San Diego

20 W. Pardue, Battelle Memorial Institute, Columbus, Ohio

21-26 Savannah River Operations Office, DOE

27-94 Savannah River Laboratory, TIS Files

96-97 Technical Information Center, Oak Ridge, TN

98 G. Linkous, Teledyne Energy Systems, Timonium, MD